



UNIVERSITY OF NAIROBI

**KENYA RIFT VALLEY BREAK-UP – FOCUS ON VELOCITY, TREND, AND
VERTICAL DISPLACEMENT**

BY:

NG'AARI JANE WAMBUI

I56/38920/2020

**A project dissertation submitted for examination in partial fulfillment of the requirements
for award of the degree of Master of Science in Geology of the University of Nairobi**

2022

DECLARATION

I declare that this project dissertation is my original work and has not been submitted elsewhere for examination, award of a degree in any other university, or publication. Where other people's work, or my own work, has been used, this has properly been acknowledged and referenced in accordance with the University of Nairobi requirements.

Jane Wambui Ng'aari

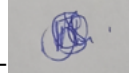
Signature

Date

-

-

-



-----2/12/2022-----

I56/38920/2020

Department of Earth and Climate Sciences

University of Nairobi

This project dissertation is submitted for examination with our approval as research supervisors.

Signature

Date

1. **Dr. Charles Maina Gichaba**

Department of Earth and Climate Sciences

University of Nairobi

maina.gichaba@uonbi.ac.ke



-----2/12/2022-----

2. **Gladys Kianji**

Department of Earth and Climate Sciences

University of Nairobi

kianji@yahoo.com



-----3/12/2022-----

3. **Professor Dr. D. S. Stamps**

Department of Geosciences

Virginia Tech

dstamps@vt.edu



-----2/12/2022-----

DEDICATION

I dedicate this project dissertation to my Mother, Mary, and three siblings, Nelson, Lilian, and Samuel. Thank you for your support.

ACKNOWLEDGEMENTS

I would like to express my gratitude and appreciation to all those who gave me their unwavering support to ensure the completion of my dissertation. Special thanks are due to my external supervisor Professor Dr. Sarah Stamps, who gave me the opportunity to take this project and diligently guided me through the training process while simulating growth experiences, diverse insights, suggestions, and encouragement while working on my dissertation. I also acknowledge my internal supervisors Dr. Charles Gichaba and Madam Gladys Kianji, alongside Dr. Edwin Dindi, who partook the crucial roles of guiding me during my write-up process, with their sincere inputs through rich perspectives, insights, revisions, and proofreading phases.

Many thanks also to all the lecturers and staff from the University of Nairobi, Department of Earth and Climate Sciences, for their efforts towards my completion and guidance to ensure a smooth sail while fabricating my dissertation. Special thanks especially to Bruce Mutegi for his help in formulations, especially at the beginning of my write-up.

I also thank my family and friends for always being there for me and giving me their endless support whenever needed.

Finally, I want to thank God Almighty because it is by His doing and Grace that I successfully went through every phase of my dissertation with courage. I will keep trusting Him in all my future endeavors.

ABSTRACT

Position time series files processed by GAMIT/GLOBK with extension velocities in the Victoria-Nubia reference frame processed by the rot program from thirteen continuous Global Navigation Satellite System (GNSS) station along the East African Rift System (EARS) from 2017 to 2021 were used to constrain plate tectonic motion to observe the Kenya rift extension rates between the Victoria microplate and the Somalian plate. These position time series files for the GNSS stations close to the major lakes along the Kenyan Rift Valley were also used to compare monthly rainfall averages from nine rainfall stations close to the GNSS stations. The GNSS stations in the Northern Kenyan Rift (NKR) showed slower extension rates with XTBI and XTBT measuring 0.8mm/yr and 2.1mm/yr velocity break-up rates respectively. On the other hand, the Central Kenyan Rift (CKR) GNSS stations showed faster extension rates with KYN6, KYN4, KYN3, KYN2, and KYN7 measuring 1.7mm/yr, 1.5mm/yr, 3.0mm/yr, 2.0mm/yr, and 3.3mm/yr velocity break-up rates respectively. The GNSS stations in the NKR show slower geodetic rifting rates unlike the GNSS stations in the CKR. The difference in the break-up velocity rates could be possibly due to the influence of Gravitational Potential Energy (GPE) that is higher in the CKR due to high topography, unlike the NKR, which is generally a depression, thus having lower GPE. The position time series also recorded surface amplitude change that portray an inverse relationship with rainfall time series. Thus, this inverse relationship shows a systematic correlation between vertical displacements portrayed by crustal subsidence and continental water loading (CWL), where increase in rainfall leads to crustal subsidence, and little or no rainfall leads to crustal flexure.

Key Words: *East African Rift System, Kenya Rift Extension Rates, Vertical Displacement, Gravitational Potential Energy, and Continental Water Loading.*

TABLE OF CONTENTS

DEDICATION	ii
ACKNOWLEDGEMENTS	iii
ABSTRACT	iv
LIST OF TABLES	viii
LIST OF FIGURES	x
ACRONYMS	xii
CHAPTER 1: INTRODUCTION	1
1.1 Background Information	1
1.1.1 Tectonic Rifting	1
1.1.2 Vertical displacement due to Continental Water Loading (CWL)	4
1.2 Problem Statement	4
1.2.1 Velocity Break-up Rates along the Kenyan Rift and Gravitational Potential Energy	4
1.2.2 Vertical Displacement due to Continental Water Loading	5
1.3 Justification/Rationale	5
1.4 Research Questions	6
1.5 Objectives	7
1.5.1 General Objectives:	7
1.5.2. Specific Objectives	7
1.6 Scope of the Study	7
1.7 Limitations of the Study	10
CHAPTER 2: LITERATURE REVIEW	11
2.1 Geology of the Study Areas	11
2.1.1 Marsabit	13
2.1.2Turkana	14

2.1.3 Nakuru.....	14
2.1.4 West Pokot.....	15
2.1.5 Samburu	15
2.1.7 Laikipia.....	16
2.1.8 Meru-Isiolo	16
2.2. Geodesy	17
2.3 Velocity Break-up rates and trends of the Victorian microplate and Somalian Plate along the Kenyan Rift Valley in the EARS.....	21
2.3.1 Rift Valley.....	21
2.3.2 Velocity Break-up Rates along the Kenyan Rift and Gravitational Potential Energy	23
2.4 Vertical Displacement due to Rifting	26
2.5 Vertical Displacement due to Continental Water Loading.....	27
CHAPTER 3: MATERIALS AND METHODS	30
3. 1 Research Design.....	30
3.1.1 GNSS Data Collection	30
3.1.2 Rainfall data for testing vertical displacement due to CWL.....	33
3.2 Data Processing	35
3.3 Analysis	35
3.3.1 GAMIT/GLOBK Output Analysis for Velocity Break-up Rates and Trends.....	35
3.3.2 Calculating for GPE as Influenced by Topography	37
3.3.3 Vertical Displacement due to CWL Analysis.....	38
CHAPTER 4: RESULTS AND DISCUSSION	42
4.1 Results	42
4.1.1 Velocity Break-Up Rates and Trends Along the Kenyan Rift between the Victoria Microplate and the Somalian Plate.....	42

4.1.2 GPE Influence on Velocity Break-Up Rates	47
4.1.3 Continental Water Loading and Crustal Subsidence	47
4.2 Discussion.....	58
4.2.1 Velocity Break-Up Rates between the Somalian Plate and the Victoria Microplate and Trends.....	58
5. CONCLUSION AND RECOMMENDATIONS.....	61
REFERENCES.....	63
APPENDICES.....	71

APPENDICES

Appendix A: General practice for NetR9's GNSS data download procedure is:	71
Appendix B: Processing using GAMIT/GLOBK.....	72
Appendix C: Using the rot program to place extension velocities in the Victoria-Nubia plate reference frame	75
Appendix D: How to check for seasonality with tsview	77
Appendix E: Calculation of Errors for Extension Velocities.....	78

LIST OF TABLES

Table 4.1 The definition of data in a psvelo file (in this case, the awk_nub_wrt_vic_keny.psvelo file).....	42
Table 4.2 Calculations from V_e and the V_n to find velocity break-up rates along the Kenyan Rift Valley in the GNSS stations	43
Table 4.3 Velocity break-up rates for the GNSS stations along the Kenyan Rift Valley with the section on the left showing the velocity break-up rates as spatially distributed along the Kenyan Rift Valley with the section on the right showing the velocity break-up rates with the spatial distribution defined by the deformation and rigid zones	44
Table 4.4 The WRMS for both annual and semiannual signals recorded the lowest values in tsview (signal 1 represents no signal, 2 represents annual signal, 3 represents semiannual signal, and 4 represents both annual and semiannual signals)	47

LIST OF FIGURES

Figure 1.1 A (Mesh geometry of the zone that encompasses the study area) B (Seismicity regions showing earthquakes of $\geq M2$) C (Deforming zones in black with the separating tectonic plates). (Stamps et al., 2018).	2
Figure 1.2 The EARS structure, including the Kenyan dome, and the triple junction near Lake Bogoria along the Kenyan Rift	3
Figure 1.3 The GNSS stations in the Northern and Central Kenyan Rift.....	8
Figure 1.4 showing the GNSS stations in their respective counties, the Kenyan Rift Valley, and the major lakes along the Rift Valley	9
Figure 2.1 Geological map of the counties with the GNSS stations, and the Rift Valley	12
Figure 2.2 A GNSS constellations. (Stamps, 2021).....	18
Figure 2.3 The principles of GNSS positioning. (Stamps, 2021).	19
Figure 2.4 How a phase measurement is conducted by a GNSS station. (Stamps, 2021).....	20
Figure 3.1 A, B, and C showing a continuous station set-up. A shows the dual frequency receiver, and battery, B shows solar panels, C shows an antenna, and D shows a Beavis point driven into a stable bedrock, although our stations were steel masts anchored in bedrock.	32
Figure 3.2 The GNSS stations, the Kenyan Rift Valley, the major lakes along the Rift Valley close to the GNSS stations, and the rainfall stations close to the GNSS stations,.....	34
Figure 3.3 The plot_velocity_hz.sh script.....	37
Figure 4.1 Velocity break-up rates for the spatially distributed GNSS stations along the Kenyan Rift Valley System.....	45
Figure 4.2 The extension trends as reflected by the GNSS stations along the Kenyan Rift Valley in a Nubia with respect to Victoria reference frame	46
Figure 4.3 A and B showing rainfall in mm/yr against time for locations close to XTBI GNSS station while C shows XTBI's position estimate time series height in meters against time	49
Figure 4.4 A showing rainfall in mm/yr against time for location close to XTBT GNSS station while B shows XTBT's position estimate time series height in meters against time	51
Figure 4.5 A and B showing rainfall in mm/yr against time for locations close to XLOY GNSS station while C shows XLOY's position estimate time series height in meters against time.....	53
Figure 4.6 A and B showing rainfall in mm/yr against time for locations close to KYN5 GNSS station while C shows KYN5's position estimate time series height in meters against time	55

Figure 4.7 A and B showing rainfall in mm/yr against time for locations close to KYN7 GNSS station while C shows KYN7's position estimate time series height in meters against time 57

ACRONYMS

EARS - East African Rift System

NKR – Northern Kenyan Rift

CKR – Central Kenyan Rift

CWL – Continental Water Loading

GNSS - Global Navigation Satellite System

GPS - Global Positioning System

GRACE - Gravity Recovery and Climate Experiment

GMT – Generic Mapping Tools

GPE - Gravitational Potential Energy

CHAPTER 1: INTRODUCTION

1.1 Background Information

As part of this geodetic research project to observe tectonic divergence in the seismically active East African Rift System (EARS), GNSS stations were installed along the Kenyan Rift in the Northern Kenyan Rift (NKR) and the Central Kenyan Rift (CKR). The data were collected for processing and used to study the velocity break-up rates along the Kenyan Rift and the trends of the plates' motion, the influence of Gravitational Potential Energy (GPE) in extension velocities, and whether continental water loading leads to crustal subsidence.

1.1.1 Tectonic Rifting

The famous EARS is an intra-continental rift system that comprises of two major segments; the Eastern, and Western Branches, as shown in Figure 1.1, that have a succession of grabens and basins. These two segments are part of a stretching rift valley from the Middle East in the north, to the south of South Africa, to the south (Prodehl et al., 1997). The systems' grabens and basins have intracontinental transfer, accommodation, and transform zones linking and segmenting (Chorowicz, 2005). A rift valley is a narrow steep-sided and flat-floored trench that scars the Earth's crust. Usually, rifts are initiated by stretching and thinning of the Earth's crust, which may be associated with upwelling mantle that forms domes that can be seen in topographical maps. The interaction with dynamic asthenosphere leads to intrusive heating and subsequent lithospheric stretching, resulting into mechanical weakening of the crust (Ebinger, 2005). Further mantle penetration leads to the brittle crust's fracture; usually three fractures that occur at 120° (National Geographic, 2022), since mechanical weakening is always the main reason leading to a continental break-up (Ebinger, 2005). The point of radiation for the three fractures is known as a triple junction, as the one seen in Ethiopia's Afar region. Therefore, crustal tension leads to plates' rifting, which comes after doming, and graben formation (Bott, 1981). The fracture in the Afar region was along the Pan-Africa suture zone (Chorowicz, 2005). In the case of the Afar triple junction, two arms, The Gulf of Aden and the Red Sea, were filled with water, while the southern arm propagated southwards to form the Main Ethiopian Rift (MER). This southern arm hosts the northern segment of the EARS, which is seismically and volcanically active, and stretches for thousands of kilometers. Interestingly, this south-trending arm divides into the Western Branch that contains East Africa's Great Lakes, and the Eastern Branch that seems to almost bisect Kenya

from the north to the south into two, further trending into Tanzania, where it has a juvenile rifting (Ring, 2014). The division between the two branches leading to a split around Lake Victoria is thought to be due to the presence of a metamorphic rock too hard for the rift to tear through that broke from the Tanzanian Craton, since the EARS generally avoids cratons as the lithospheric scale extension follows prehistoric north oriented Mozambique Belt sutures (Chorowicz, 2005).

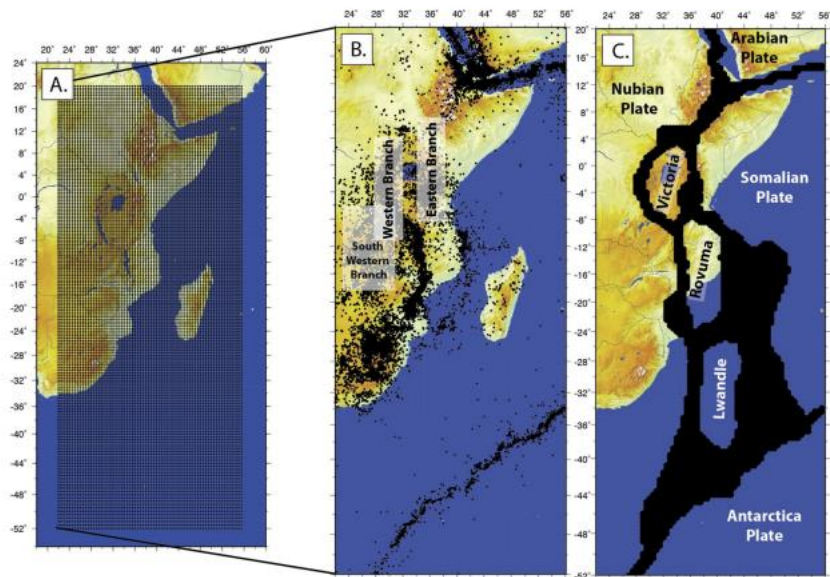


Figure 1.1 A (Mesh geometry of the zone that encompasses the study area) B (Seismicity regions showing earthquakes of $\geq M2$) C (Deforming zones in black with the separating tectonic plates) (Stamps et al., 2018).

In Kenya, the EARS runs throughout the country in a roughly north-south structural configuration. This graben system's structural orientation was established by volcanism and a ENE-WSW to east-west extension orientation during the Miocene period (Riedl et al., 2020). The Rift system in Kenya is divided into three rifts, the NKR, the CKR, and the Southern Kenyan Rift (SKR), and they correspond to the Kenyan dome, as illustrated in Figure 1.2. The NKR is situated in the Northern part of the dome and composed of two parallel rifts separated by the Kamasia Block and both trending at $N10^{\circ}E$ (Chorowicz, 2005). This northern rift propagates southwards from the southern Lake Turkana half graben to Lake Bogoria. In contrast, the CKR is defined by end of the northern rift and a sharp orientation change as it trends in the $N150^{\circ}E$. Near Lake Bogoria, which is a triple junction (to the northern, central, and the Nyanza rift) and close to the central Kenyan dome, branches the Nyanza half-graben that's trends $N80^{\circ}E$ (Chorowicz, 2005).

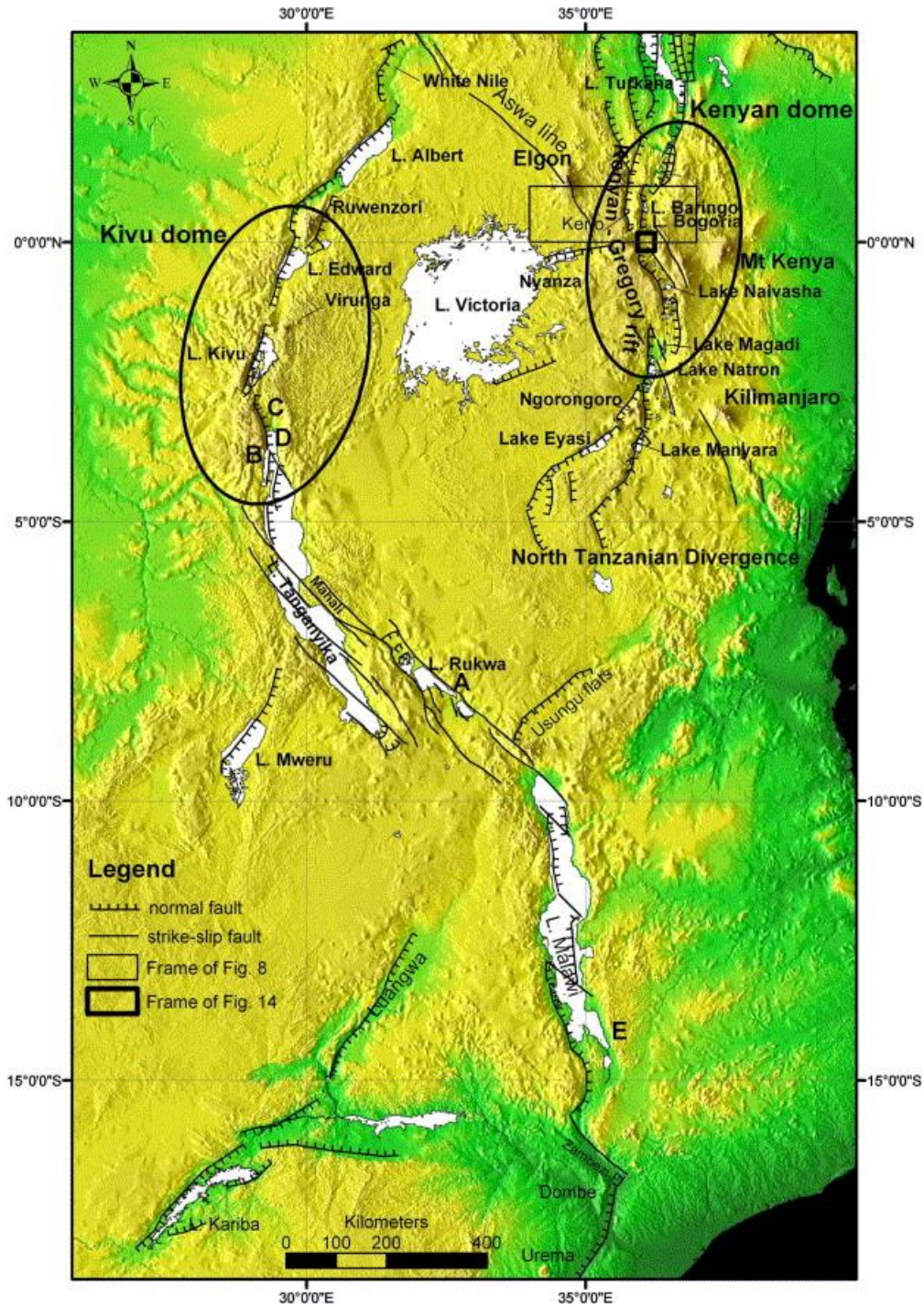


Figure 1.2 The EARS structure, including the Kenyan dome, and the triple junction near Lake Bogoria along the Kenyan Rift (Chorowicz, 2005)

The historically known African plate is currently breaking into two major plates, the Nubian and the Somalian plates, along the rift valley with a southernmost San plate also breaking

off from the Nubian plate (Wedmore et al., 2021). In Kenya, the extension is accommodated by the topographical features along the Rift Valley, with the Kenyan rift along the EARS dividing the Victoria microplate from the Somalian plate. The rate at which this regional lithospheric extension is happening varies along the EARS. Additionally, while the EARS is one of the famous rifts scaring the Earth with most of its dynamics and kinematics known, less is known about the Kenyan rift in terms of extension. While this might be attributed to minimal data and prior lack of Global Navigation Satellite System (GNSS) coverage in the area, this study helped shed light on the extension mystery along the Kenyan Rift by evaluating the velocity break-up rates and tectonic plate trends.

1.1.2 Vertical displacement due to Continental Water Loading (CWL)

The lakes along the EARS are flooding at an unprecedented speed causing alarm in the scientific community (Ministry of Environment and Forestry, 2022). This mystery is astounding since it is a regional phenomenon observed in both the Eastern and the Western Branches of the Rift Valley. In the Western Branch, the alarming lake level rise are causing adversities in Uganda, Burundi, and Congo, because they are displacing families (Baraka, 2022). In agreement, Rédaction Africanews (2021) reported that Lake Tanganyika is getting deeper due to deforestation and impacts of climate change in the highland and water catchment areas. This is an occurrence that has been experienced during the recent decade even though substantial rise was experienced during the end of 2019 and the start of 2020. This occurrence coincides with the increased average rainfall that drained into the lakes in East Africa in 2019, recording one of the wettest observed periods that led to regional flooding. Interestingly, as rainfall increases and more water is drawn into lakes, continental water loading (CWL) occurs. According to Birhanu & Bendick (2015), this mass water loading is sufficient to cause solid Earth response through varying amplitude displacement. This study will therefore seek to assess outputs from GNSS observations to understand if vertical displacement, which confirms crustal subsidence, is due to meteorological factors.

1.2 Problem Statement

1.2.1 Velocity Break-up Rates along the Kenyan Rift and Gravitational Potential Energy

Along the EARS, the historically referenced African plate is breaking into smaller microplates and plates creating a rift extension. On the Eastern Branch of the EARS, the Somalian plate is slowly pulling apart from the Victoria microplate along the ENE-WSW to east-west

extension orientation (Riedl et al., 2020) intra-continental axial rift. However, the extension rates between the NKR and the CKR vary, and the variations are not known. Ebinger (2005) and Stamps et al. (2008, 2021) in their articles claim that the break-up velocity rates increase northwards. The difference in this extension rate is attributed to topographical differences since GPE plays a significant role in controlling the extension style (Knappe et al., 2020) through varying strain accommodation in the laterally heterogeneous Earth's crust. GPE is the gained energy by an object raised against the Earth's gravitational pull to a certain height, and it increases with increase in height. Therefore, the difference in the velocity break-up rates based on the fact that areas with high GPE have higher extension rates compared to areas with low GPE. Therefore, it is likely that the NKR has low GPE compared to CKR, due to topographical differences, a factor that should be considered while studying the varying extension rates.

1.2.2 Vertical Displacement due to Continental Water Loading

With the continuous extension along the Kenyan Rift, the string of lakes along the Rift Valley (Lake Turkana, Lake Baringo, Lake Bogoria, and Lake Nakuru chosen for the study) have recently been recording increased water levels. This phenomenon coincides with increased average rainfall in the highlands and catchment areas of East Africa (Rédaction Africanews, 2021; Avery, 2020; Baraka, 2022). Additionally, the GNSS stations close to these lakes show crustal subsidence. This is in line with Jiang et al. (2013), Birhanu & Bendick (2015), and Birhanu et al. (2018) who agree that continental water loading leads to crustal subsidence. However, this phenomenon is not confirmed along the Kenyan Rift due to lack of recent precise data, a case that this study sought to answer using precise geodetic data in comparison with rainfall data.

1.3 Justification/Rationale

Regional rifting along the Kenyan Rift is a known phenomenon that initiated during the Miocene period. While a lot is known about the Kenyan Rift's structural geology, little information is known about the Kenyan Rift's geodynamics and kinematics using precise geodetic tools due to poor GNSS coverage along the Eastern Branch of the EARS (Stamps et al., 2018). Therefore, very limited literature exists on the complex Victoria microplate and Somalian plate extension evolutions. However, Knappe et al. (2020) did a geodetic research study with GNSS coverage in Northern Kenya in the Turkana depression and found high strain rates along the extension. Even so, there is not any recent geodetic research studies done on the complex CKR. As a result, there

is a lack of crucial scientific knowledge about the evolution of the Kenyan Rift, in both varying velocity break-up rates and trends, as influenced by GPE.

In recent years, the string of lakes along the Kenyan Rift have recorded an increase in water levels. This phenomenon has led to the mass displacement of communities close to the lakes and destruction of property. The increase in lake levels occur at periods of increased average rainfall. This occurrence remains a puzzle to the science community and little is known about the cause. As a result, many people have come up with hypotheses about what could be the possible cause. Some hypotheses are that the rise in lake levels are due to meteorological factors, or that it could be related to the rifting process along the EARS, or that it is a climate change phenomenon (Avery, 2020; Baraka, 2022). Despite this change in lake levels, there is an observed crustal subsidence in the string of lakes along the Kenyan Rift Valley that accompany the above average rainfall but without robust evidence of correlation.

Therefore, this project on rifting along the Kenyan Rift and the influence of continental water loading along the Rift Valley had the objective of explaining how rifting varies along the Kenyan Rift by correlating velocity break-up rates in the NKR and the CKR, alongside influence of the GPE. The study was also expected to shed light on the causes of crustal subsidence along the rift and whether they are related to increased rainfall, which might be a cause of increasing lake levels. This project was also crucial since it applied geodetic techniques to achieve its objectives. Geodesy, which exploits remote sensing techniques, is a new applied technology of Earth sciences in Kenya that has not been essentially exploited in the past to study aspects like plate motion constrains, groundwater, and gravity, just to mention a few. Therefore, this research project will catapult the need for scientists to exploit this technology for research purposes. It will also help policy makers and the communities living close to the lake to be aware of the impending natural disasters and adequately prepare to mitigate the negative impacts.

1. 4 Research Questions

- i. How do the break-up velocity rates between the Northern and the Southern Kenya Rifts differ? Is this difference influenced by GPE?
- ii. Is the crustal subsidence observed along the rift related to meteorological factors that cause continental water loading due to lake level rise?

1.5 Objectives

1.5.1 General Objectives

- i. To constrain plate motions along the EARS using GNSS stations as a means of understanding rifting rates along the Kenyan Rift.
- ii. To analyze rainfall data from stations close to lakes along the rift to understand its potential influence on crustal subsidence in relation to continental water loading.

1.5.2. Specific Objectives

- i. To determine the difference in velocity break-up rates between the Victoria microplate and the Somalian plate with a focus on the Northern and the Central Kenyan Rifts
- ii. To determine the role of GPE in differentiating the break-up velocity rates between the NKR and the CKR
- iii. To determine the effects of meteorological factor (in this case rainfall) on crustal subsidence due to continental water loading along the rift

1.6 Scope of the Study

The study areas are located in the Northern and Central Kenyan Rifts. The NKR is bounded by the coordinates (34.024°E, 4.584°N), (38.815°E, 4.600°N), (34.059°E, 1.949°N), and (38.821°E, 1.955°N), while the CKR is bounded by the coordinates (34.059°E, 1.949°N), (38.821°E, 1.955°N), (34.010°E, 0.983°S), and (38.797°E 0.983°S). The specific thirteen GNSS stations (XTBI, XTBT, XLOY, XLOK, XHOR, XSAS, KYN1, KYN2, KYN3, KYN4, KYN5, KYN6, and KYN7) were located in Marsabit, Turkana, Nakuru, West Pokot, Samburu, Baringo, Laikipia, Meru, and Isiolo counties, as shown in Figure 1.3 and Figure 1.4. Raw geodetic data from 2017 to 2021 in the form of RINEX formats from dual frequency GPS receivers were retrieved from UNAVCO archives (www.unavco.org, doi:10.7283/T5SN077J, doi:10.7283/T5WS8RKK, doi:10.7283/T5XD0ZZG). Additionally, rainfall data were acquired for the corresponding years from the Kenya Meteorological Department (KMD) for comparison with the tsview modelled station position time series vertical displacements from GAMIT/GLOBK processing.

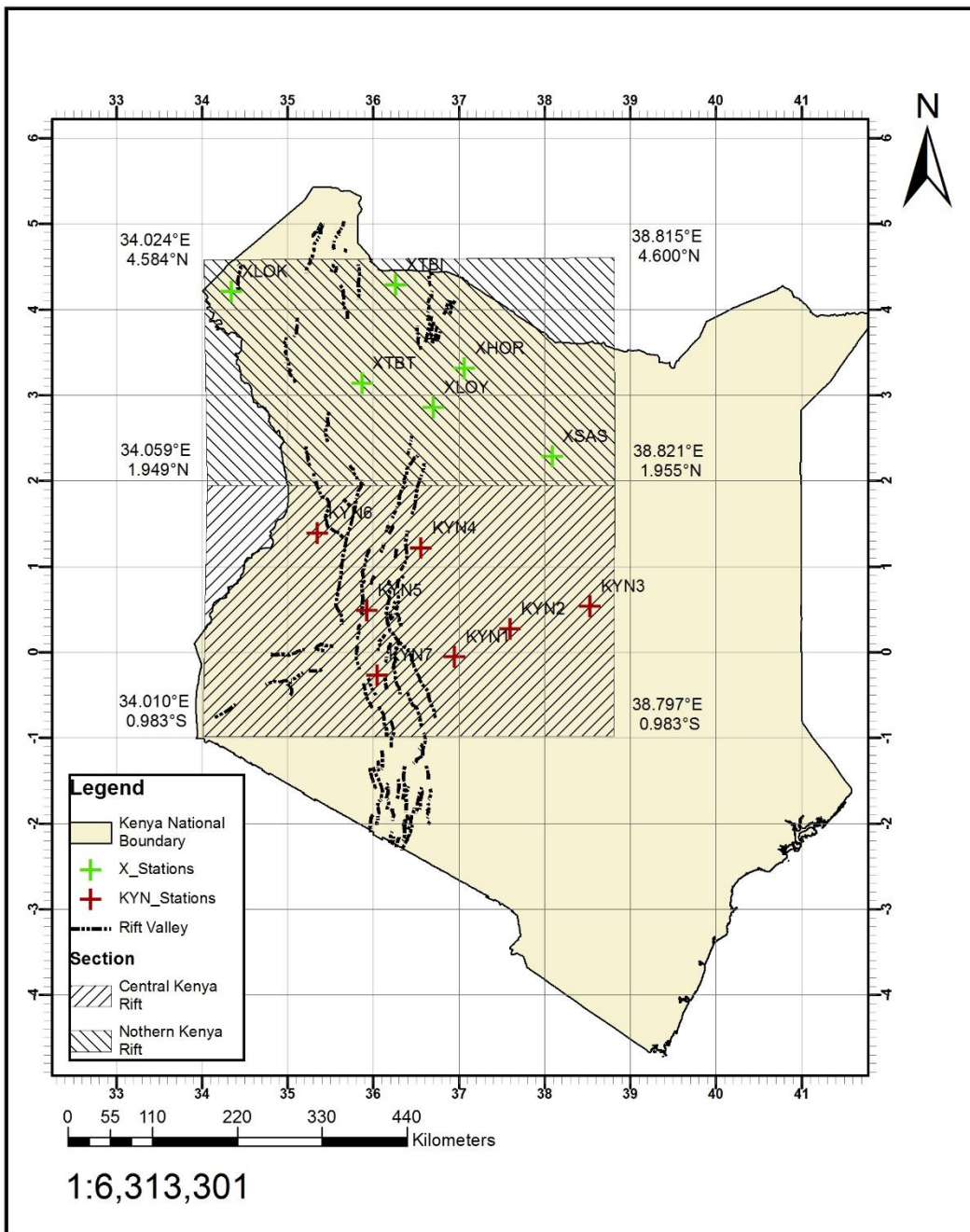


Figure 1.3 The GNSS stations in the Northern and Central Kenyan Rift

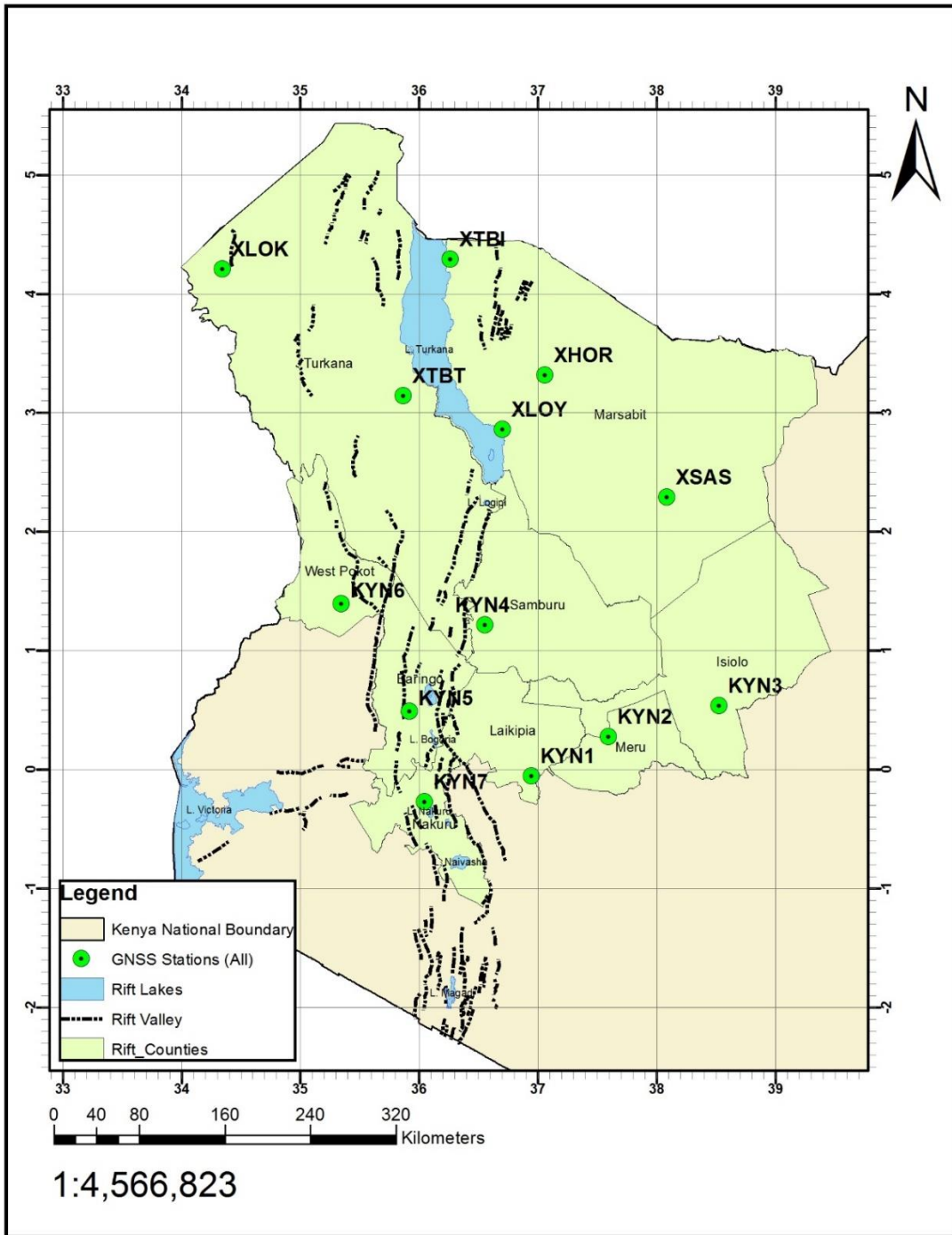


Figure 1.4 The GNSS stations in their respective counties, the Kenyan Rift Valley, and the major lakes along the Rift Valley

1.7 Limitations of the Study

One of the primary limitations was the gaps in the geodetic data since some stations went down for some time before they were repaired, leading to inconsistent data. Additionally, insecurity and accessibility impacts, especially in Northern Kenya, limited the amount of GNSS coverage along the Eastern Branch. It was also assumed that the regional effect of continental water loading would have a direct impact on the Beavis points driven into the bedrocks. Finally, the coordinates binding the NKR and the CKR had a direct effect on the area of the regions used to calculate for GPE. Therefore, the influence of the used coordinates to bind the study areas led to ambiguities in the calculated GPE values.

CHAPTER 2: LITERATURE REVIEW

2.1 Geology of the Study Areas

Kenya's general geology is composed of the oldest Archaean rocks defined by the Nyanzian meta-volcanics and Kavirondian meta-sediments. The Archaean rocks are succeeded by the Proterozoic rocks that include the Mozambique Belt and the Bukoban series. The Palaeozoic, also called the Mesozoic sediments, succeed the Proterozoic rocks, which are characterized by faulting and rifting. One of the major geologies of Kenya are along the Rift Valley, and they are composed of the Quaternary/Tertiary volcanics that mostly cut across the Mozambique Belt. Finally, the youngest rocks are the Pleistocene to recent soils, due to the process of weathering and erosion.

A detailed geology of the counties with the GNSS stations is illustrated in figure 2.1

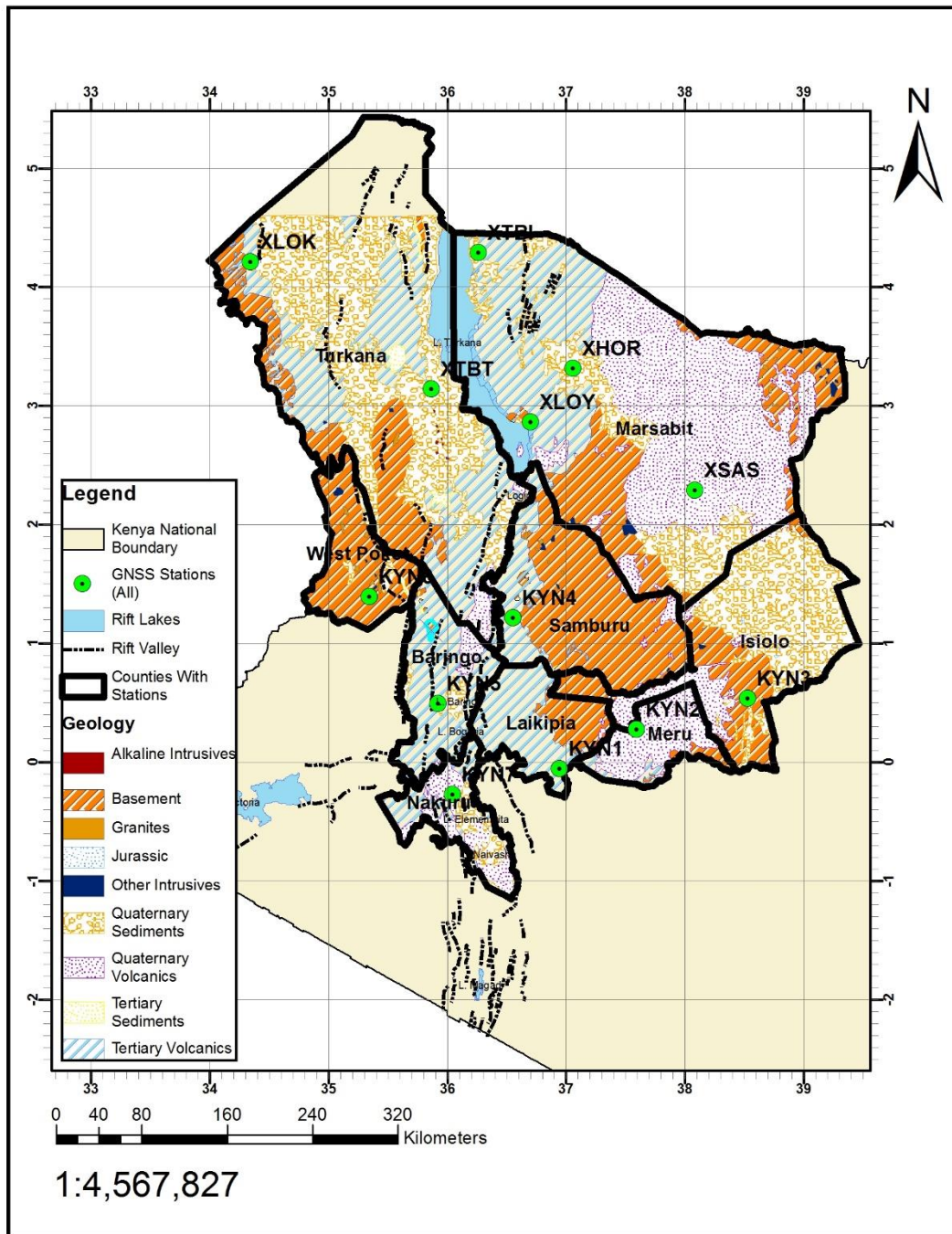


Figure 2.1 Geological map of the counties with the GNSS stations, and the Rift Valley (Githaiga et al., 2021)

2.1.1 Marsabit

Marsabit County is located off the center of the EAR in an arid scene of a massive basaltic shield volcano composed of basaltic rapilli breccia volcanic ash and cinder cones that interlay with extensive olivine basalt flows on a Precambrian basement of metamorphic rocks (Kasabuli, 2016). The county is covered by volcanic plateaus and shields, and a Sub-Miocene Chalbi Basin filled with unconsolidated superficial sediments (Key, 1987). A series of volcanic activities took place to ultimately form the shield volcano with initial lava, forming lateral thin and extensive fissure-controlled basal basalts. These volcanic episodes, started during the Pliocene, the same time as the commencement of the rifting, and carried on to the Quaternary period, respectively (Kasabuli, 2016).

The county's geomorphology is evident from six recognized physiographic provinces. These provinces include the four mature Tertiary from the Paleogene but slightly modified during the Quaternary central and southern lowlands in Korante plain, Hedad, Koroli Desert, and Chalbi Basin, and the two north-western and eastern immature Cenozoic shield volcanoes. The four mature provinces experienced a Pre-Late Miocene erosional episode in the NW orientation, leading to the formation of the SW slope. This erosional episode led to the formation of the Chalbi Basin argillaceous unit since it corresponded to the axial trough. However, this was preceded by a late Miocene volcanic activity that formed the basalt plateaus in the area. Later during the Pliocene, there was a major erosion that led to the formation of sand dune fields. This major erosion led to the formation of drainage channels, and ultimately, Lake Chalbi. The county is also defined by NW and E volcanic provinces from the Plio-Pleistocene volcanism. Additionally, the county is defined by 180 cinder cones and 200 maars. These cinder cones were formed after erosion of unstable volcanic features during the Holocene period.

However, there were intervals of pyroclastics accumulations from the maars and cinder cones during the subsequent Quaternary eruption episodes with faulting from volcanism. Later, erupting thin extensive olivine basalts from the cones concealed the major faults (Kasabuli, 2016). As a result, Marsabit is underlain by Pre-Cambrian metamorphic rocks to the north eastern and south western side, covered by tertiary and Pleistocene volcanic sheets and rocks on the north eastern and central sides, and recent Quaternary sediments occupy the south western plains and cover the seasonal Lake Chalbi (County Government of Marsabit, 2013). The Precambrian

metamorphic rocks exposure is due to the erosion of the volcanic and sediment cover (Earthview Geoconsultants Limited, 2008). Therefore, the land is defined by deserted residual hills, dissected plain surfaces, and lava-caped plateaux that rise the plain approximately 50 – 200 feet (Randel, 1970).

2.1.2 Turkana

The Turkana County that covers about 131,000 km² of Southern Ethiopia and Northern Kenya is a sedimentary basin and hydrographic system with a long but detailed and well-preserved Rift Valley geology, cultural development, and biotic evolution in its strata (Feibel, 2011). The Turkana Basin is a significant part of the EARS and much of it is encompassed in the Kenyan and Ethiopian domes. The start of the basin formation was associated with the northwest-southeast oriented Central African Rift System (CARS) from the Jurassic-Paleogene period (Feibel, 2011). The CARS basin was preserved from the late Cretaceous and remained significant through to the Miocene period, and significantly influenced sediment deposition and accumulation in the Turkana Basin. However, during the Early Pliocene period at the commencement of the EARS subsidence, the Turkana Basin was delineated to its presently trending north-south half-graben systems (Feibel, 2011). The geological succession is composed of a basement of metamorphic rocks from the Neoproterozoic to Cambrian period as part of the Mozambique Belt. The Basement system is covered by volcanic successions and volcanic rocks cover the larger Turkana Basin portion. The volcanic rocks with considerable thicknesses that cover the expansive basin are extensive basalts, rhyolites, and trachytes. Finally, the county has a rich strata of sedimentary rocks, with the oldest units having accumulated in the CARS. These sedimentary rocks range from conglomerates to Cretaceous sandstones that started accumulations from the Oligocene period to the Plio-Pleistocene age (Feibel, 2011).

2.1.3 Nakuru

In the remarkably complex Central Kenya's Rift Valley inner graben lies Nakuru County, a region that for the last 6.2 Ma, has continuously experienced trachyte magma eruptions (Leat, 1991). Prior to the first sub-Miocene eruption, the floor warped down (McCall, 1967). The stratigraphy of the area, starting from the oldest rock, include the Bahati Trachytes and Tuffs, Meroronyi Tuffs, Mbaruk Basalts and Trachytes, Sirikon Trachyte Lava and Tuffs, Menengai Volcanics, Bahati Sediments, Elementaita Basalts, Tuffs, Lacustrine and Fluvial Deposits, and the

Alluvium, Trona Impregnated Silt (Conti et al., 2021). However, the county has five major identified trachytic rocks which include voluminous ignimbrites, lava flows, strombolian deposits, extensive air-fall deposits, and hydromagmatic tuff cone deposits (Leat, 1991). Even so, despite the thick volcanic sequence, the county's ancient basement system from the Precambrian period composed of schists and gneisses emerge at the Rumuturi Plain (McCall, 1967). Amid historic volcanism, Nakuru area has experienced a series of faulting, with major faulting occurring during the Upper Tertiary, lower Quaternary, and Middle Quaternary periods. Presently, the area is covered by recent superficial deposits composed of soils and alluvium, and hot spring travertine deposits due to its rich network of hot springs (McCall, 1967).

2.1.4 West Pokot

West Pokot County is a generally mountainous area with undulating hills rolling across the county. However, one can see escarpments that define the county's topography. West Pokot is positioned on the metamorphic basement system from the Precambrian period. These phaneritic-textured metamorphic rocks are primarily composed of gneisses, schists, and foliated metagranites. Some of the primary minerals in these rocks are biotites, hornblendes, feldspars, and quartz. However, the county is also defined by some volcanic rocks that overlie the basement system and outcrop in some parts. These volcanic rocks include dykes and pegmatites. Additionally, recent alluvial deposits that form the unconsolidated sedimentary unit of the area are found along the county's dry river courses.

2.1.5 Samburu

Samburu County is dominantly marked with its prominent range of mountains, hills, and foot slopes oriented in the NNW-SSE direction. The county has a Precambrian basement system of metamorphic rocks significantly composed of granites and gneisses (Touber, 1989). The county's main topography, a spectacular scenery of the Rift Valley escarpment, also consists of uplands and undulating plains defined by Tertiary and Quaternary volcanic flows and fluvial and lacustrine sediments that form plateaus along the normal faults. This peneplain from the sub-Miocene period overlays the Precambrian basement (Makinouchi et al., 1984). However, due to the significantly varying climate in the county, the sedimentary units composed of alluvial sediments vary in thickness from place to place (Touber, 1989). As a result, altitude and terrain thickness cause a significant variation in soil coverage of the area.

2.1.6 Baringo

One of the prominent features in Baringo County is the Kerio Valley on the western side, while Lake Baringo and Lake Bogoria are on the eastern side. The county's location along the Central Kenyan Rift Valley System gives it a complex geology. The county has a trend of hills, majorly covered by volcanic rocks (Baringo County, 2013). Alongside the formation of these volcanic rocks, intense tectonic activities along the rift with erosion and sedimentation periods occurred from the mid-Miocene period (Institute of Hydrology, n.d.). The county's geology can be broadly divided into two; the volcanic complex and the main Lake Baringo and Bogoria Rift Valley, and the Kerio Valley. The Volcanic complex, which is only part of the main Rift Valley, is primarily composed of volcanic rocks, which are basalts, phonolites, trachytes, and tuffs. On the other hand, the Kerio Valley and Lake Bogoria's and Baringo main Rift Valley have alluvial and lacustrine sediments from the Quaternary period. Additionally, while recent tectonic activities have been primarily restricted in the Bogoria-Baringo basin, the county generally has tensional faults in the north-south orientation (Institute of Hydrology, n.d.).

2.1.7 Laikipia

Laikipia County lies on the old Precambrian Basement System composed mainly of gneisses defined by broad banded structures, and homogenous granites and migmatites. These metamorphic rocks are primarily composed of quartz and feldspars alongside accessory biotite and hornblende minerals. These metamorphic basement rocks are overlaid by volcanic lava and deposits. The volcanic formations in the county include phonolitic lava sheets, Nanyuki volcanic sediments, sirimon formation lavas, ashes, and mudflows, and basaltic lavas (Ahn & Geiger, 1987). The alluvium soils in the county are of volcanic origin and formed during the Quaternary period.

2.1.8 Meru-Isiolo

Meru and Isiolo counties are underlain by the complex Basement system significantly composed of metamorphic gneisses, quartzites, and schists from the Precambrian period. Volcanic rocks overlay the basement system. This volcanic complex is composed of Tertiary volcanic rocks that erupted between the Miocene and the Pliocene periods. The Quaternary volcanic rocks and sediments of the Pleistocene period are also part of the volcanic complex. The alluvium deposits of the counties that occur along streams are also of the Pleistocene to recent ages. These alluvium

deposits are composed of silt, sand, and gravel (Nippon Koei Co., Ltd. & Nihon Suido Consultants CO., Ltd., 1997). However, these volcanic rocks can be classified into two major series: the Mt. Kenya volcanic series, and the Nyambeni volcanic series. The Mt. Kenya volcanic series from the bottom consists of lower basalts which have kenyte and tuff, upper olivine basalts, and parasitic vents tuffs, basalts, and ashes. The Nyambeni volcanic series on the other hand from the bottom is composed of lower Nyambeni lavas, upper Nyambeni lavas, and parasitic vents phonolites, basalts, tuffs, and ashes (Mason, 2007).

2.2. Geodesy

Formerly known as University NAVSTAR Consortium, UNAVCO, a non-profit university-governed consortium, is a community of scientists who use geodesy to understand the Earth's processes and hazards. UNAVCO (n.d.), which is also a data source for geodesists, defines geodesy as the science of everything from coordinate systems under positioning and navigation used to measure extremely precise shape, gravity, and orientation of the Earth. Therefore, geodesy is applicable in measuring moving tectonic plates, warning signs of eruptions, shrinking glaciers, rising sea levels, and overuse of groundwater, especially during droughts, just to mention a few. Some of the crucial tools used in geodesy include satellites. According to May (2014), a satellite is a machine, moon, or planet that orbits a star or another planet. For example, the Earth is a natural satellite. However, there are other man-made satellites that are used for communication. A group of many satellites form a GNSS, which has its unique satellites' constellation that provide the desired coverage from arranged orbits (Stamps, 2021), as shown in Figure 2.2.

The GNSS has three segments. The first segment is the space segment and it is composed of satellites. This segment broadcasts radio signals for users who receive the signal commands on Earth. A satellite sends unique signals that identify it and give its orbit, status, and time. Currently, the global and regional GNSS constellations include Global Positioning System (GPS) of the United States, GLONASS of the Russia Government, Galileo of European Global Navigation Satellite Systems Agency (GSA), BeiDou, also COMPASS, of China, The Indian Regional Navigation Satellite System (IRNSS) of India, and finally Quasi-Zenith Satellite System (QZSS), also known as Michibiki, of Japan (Stamps, 2021).

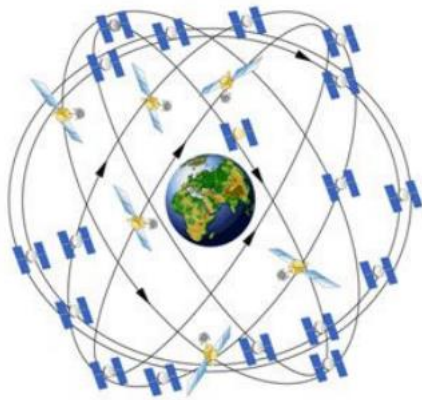


Figure 2.2 A GNSS constellations. (Stamps, 2021)

The second segment is the control segment, which basically maintains the space segment. The control segment has two primary functions, sending commands to satellites, and monitoring the space segment. Finally, the third segment is the user segment. This segment is always on Earth and it has receivers that record the signals from the space segment. The user segment also interprets the radio signals as broadcasted by the satellites (Stamps, 2021). Some examples of the user segment include mobile phone, GPS receivers, and trackers.

Satellites, which are launched into space about 20,000 km above the Earth using rockets, orbit the Earth at different heights, speed, and paths. The Earth's gravity pull balances the satellites, making sure they orbit at a balanced speed in their appropriate paths. Otherwise, the satellites would not adhere to an orbit and get lost into space or fall back to Earth in a straight path. Amazingly, the positioning of the satellites allow for a bird's-eye view, thus making it possible for them to collect more data over a vast geographic area (May, 2014). This aspect makes the process of collecting data using satellites to be classified under remote sensing.

Remote sensing is the observing of some phenomenon from a distance (USGS, n.d.). The concept of remote sensing is embedded in the electromagnetic spectrum since optical remote sensing satellites rely on reflected light from an object on Earth to detect their corresponding electromagnetic energy (USGS, n.d.). The satellites' sensors collect and record the energy information, then transmit them to a receiving station where they are processed into colored images.

The GNSS positioning principles are intricately in the form of speed, distance, and time.

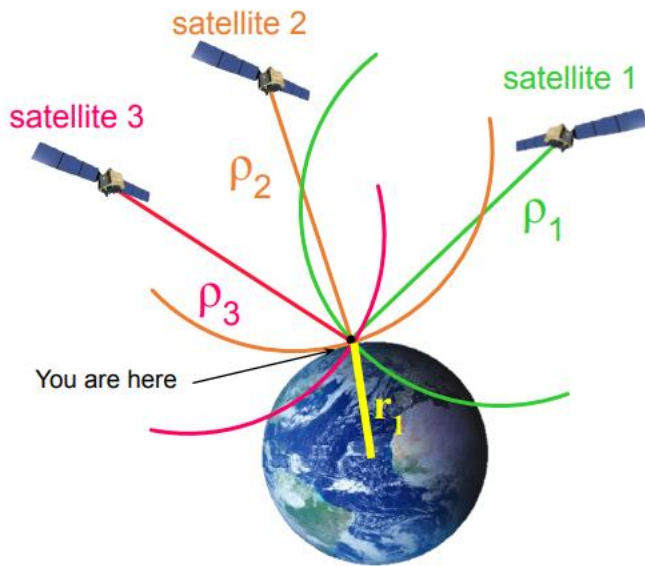


Figure 2.3 The principles of GNSS positioning. (Stamps, 2021).

In this case, as illustrated in Figure 2.3, if Satellite 1 sends a signal at time t_s , then the ground receiver will receive the signal at time t_r . Therefore, the range measurement ρ_1 to satellite 1 will be $\rho_1 = (t_r - t_s) \times \text{speed of light}$

However, if the position of the satellites in an Earth-fixed frame (X_s, Y_s, Z_s) is known, then we measure the observable range as (Stamps, 2021):

$$\rho_r^s = \sqrt{(X_s - X_r)^2 + (Y_s - Y_r)^2 + (Z_s - Z_r)^2} \quad \dots\dots\dots \text{Eq:2.1}$$

To measure the less precise pseudorange, the equation used is: propagation time $(t_r - t_s)$, multiply by $c = \text{“pseudoranges”}$, where c is the speed of light in a vacuum (Stamps, 2021).

At least 4 of these pseudoranges acquired at the same time are required to calculate position (longitude, latitude, time, and height).

The GPS signal has various characteristics. Satellites have atomic clocks aboard. These atomic clocks produce a fundamental frequency (f_0) of 10.23Mhz. However, two frequencies, L1 and L2 used to transmit information from the satellites can be derived from f_0 ; L1 ($f_0 \times 154$) =

1.57542 GHz with 19.0 cm wavelength, and L2 ($f_o \times 120$) = 1.22760 GHz with 24.4 cm wavelength. This information is always in the binary format of 0s and 1s. These binary values change creating varying rates which are referred to as chip rates. These rates create the pseudorandom noise codes (PRN codes) which are unique to each satellite (Stamps, 2021). The navigation messages in the GPS signal include the system status, the satellites drift and clock offset, the ephemerides (calculated satellite positions at regular intervals), and ionospheric correction parameters.

The GPS signals are always decoded by receivers. The receivers can always be single-frequency or dual-frequency radio frequency receivers. Single-frequency receivers have L1 while dual-frequency receivers have both L1 and L2. One of the primary information that receivers decode are phase measurements. Phase measurements are done through comparison of the incoming signal to the receiver and the replica that the receiver creates of the incoming signal. These comparisons made are of the code measurements, which are then correlated to measure the shift between the two signals. The time shift between the two signals signifies the time needed for the signal to travel from the satellite to the receiver (Stamps, 2021).

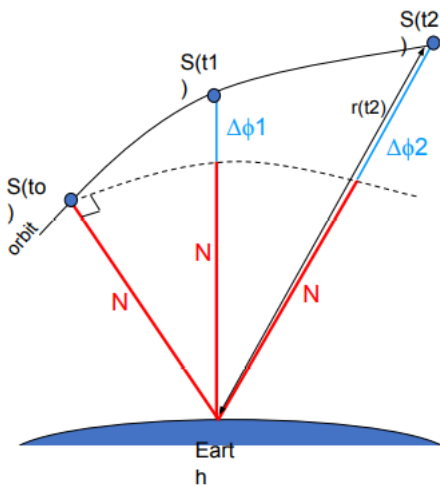


Figure 2.4 How a phase measurement is conducted by a GNSS station. (Stamps, 2021).

The concept in Figure 2.4 is based on a satellite's movement from t_0 to t_2 . At t_0 , a GNSS station on Earth starts tracking the satellites incoming phase signal which is unknown, but assumed to be N . As the satellite moves, the GNSS station receiver counts the real number of phases as time functions. However, by the time the satellite gets at t_2 , N will still be the same if there was no loss

of lock. Founded on this, the equation for phase measurement, which is the primary equation in GAMIT/GLOBK for positioning for precise positioning at the millimeter level, is (Stamps, 2021)

$$\Phi_i^k(t) = \rho_i^k(t) \times \frac{f}{c} + (h^k(t) - h_i(t)) \times f + ion_i^k(t) + trop_i^k(t) - N_i^k + \varepsilon$$

.....Eq:2.2

Where;

t = time of epoch, i = receiver, k = satellite, ρ_i^k = geometric range, h^k = satellite clock error, h_i = receiver clock error, ion_i^k = ionospheric delay, $trop_i^k$ = tropospheric delay, N_i^k = phase ambiguity, ε = phase noise

Phase measurements are very precise and can also be used to measure the satellite-receiver distance when multiplied by the wavelength.

The GPS receivers record five observables; L1 and L2 phase observables as derived from L1 and L2 frequencies, course acquisition (L1 only) and precision (both L1 and L2) pseudorange observables, and navigation messages (Stamps, 2021). These observables are stored in a binary proprietary format known as the Receiver Independent Exchange (RINEX) format.

The GNSS strategy using phase measurements has more accuracy than using pseudorange only. The phase measurements have high precisions that vary from <1mm to 10 cm. These precision variations depend on processing strategies including the ionosphere, troposphere, and orbits. Additionally, phase measurements can only be post-processed due to the need of reference stations' phase measurements too. This leads to differential GNSS since a reference station's position is precisely known (Stamps, 2021).

2.3 Velocity Break-up rates and trends of the Victorian microplate and Somalian Plate along the Kenyan Rift Valley in the EARS

2.3.1 Rift Valley

Tectonic features in axial rift-designed intra-continental ridge system of the EARS are significantly related to volcanism. Chorowicz (2005) claims that crustal up-warping during the 15 Ma period succeeded the arrival of a mantle plume that subsequently led to partial melting beneath the lithosphere. This partial melt effect was related to a moderate Earth uplift caused by the asthenospheric mantle ascension. Chorowicz (2005) further states that the uplift caused by the

plume effect led to more thermal ductile thinning in the Kenyan rift crust, a process that led to the failure in the Afar region that propagated southwards along the crustal suture zone along the MER. However, since the MER and the northern Kenyan rifts could not link since they followed different Pan-African suture zones, the southern propagation formed the graben basins in the Omo-Turkana region. As a result, the break from the Afar region created regions with different crustal thicknesses; about 20 km in the Turkana basin, about 51 km in the western and eastern MER plateaus, about 35 km in the southern Lake Baringo region, and approximately less than 31 km in the Omo basin. Therefore, the break-up led to varying topographies where some areas have thicker crusts than others. This is crucial since with varying topographies and crustal thicknesses are linked with varying GPE, leading to varying break-up velocity rates.

Over the years, there have been debates and unanswered questions on what powers continental break-ups. Usually, mechanical weakening is always thought as the main reason leading to a continental break-up. According to Ebinger (2005), primary reasons for crustal weakening are intrusive heating, lithosphere stretching, and interaction with dynamic asthenosphere. The author explains two continental break-up models, Model A and Model B, which can be used to explain the rifting. Model A applies the purely mechanical perspective while Model B involves asthenosphere-lithosphere models coupled by magmatism. In Model A, strain leading to rupture depends on rheology where it may be accommodated by localized significant offsets in brittle layers or ductile deformation in weaker layers across a broad zone. However, in Model B, rupture strain is accommodated through magmatic injections like dykes in lower ductile crust with fractures on the surface. Keen (1985) agrees claiming that rifting driving forces fall into either active rifting where the lithosphere is rifted by the asthenosphere's energy, or passive rifting where lithospheric extensional stresses play the primary rifting role. Ebinger (2005) further mentions that magmatic penetration into the layers leads to heat transfer which subsequently weakens the plate, resulting to further weakening. According to the author, there is magmatic intrusion in the Kenyan Central Rift Valley that led to the lithosphere stretching by about 10 km and thinning by about 90 km. This is confirmed by refraction and tomography seismic low-velocity mantle velocity information showing a fraction of small melt in the mantle while the crust in the central rift with narrow high velocity zones show the presence of cooled melt intrusions. Also, high velocity and density material in a central zone by gravity and seismic reflective data prove

the presence of solidified mantle intrusion in the upper crust and presence of frozen melt at the crust-mantle boundary.

2.3.2 Velocity Break-up Rates along the Kenyan Rift and Gravitational Potential Energy

As the EARS propagates south, it encounters the thick, strong, and cold Tanzania craton that probably deflects the Rift Valley. Gravity-topography relations show that strong lithosphere underlies the Tanzania craton rather than the younger surrounding belts, with the weakest lithosphere being the stretched rift valleys to the south. The southern cold Tanzania craton encountered by the EARS might be crucial in delineating why the velocity rates are lower in the southern EARS compared to the northern EARS. This is because the rifting rate by geodetic data predict a 6-7 mm/yr opening rate in the N90–109° direction with the extension occurring on both the Western and Eastern Rift Systems (Ebinger, 2005). Thus, the large Nubian plate is trending NNW about the south Atlantic rotation pole. Stamps et al. (2015) agree claiming that the EARS relative divergent motion increases from the south to the north, with the Afar triple junction region recording higher rates of 6 mm/yr, as backed by paleomagnetic observations. The authors further add that the relative motion of the Somalian plate indicates a clockwise direction respective of an offshore South Nubian pole.

Stamps et al. (2018) studied strain rates in zones from the Afar region and those along the Eastern and Western Branches. They improved the SSA-GSRM v.2.1 to a new Sub-Saharan Africa (SSA) GSRM v.1.0, GEM global geodetic strain rate model to resolve for previously unseen spatial heterogeneities along the EARS. The only new data incorporated into the SSA-GSRM v.2.1 model was new GNSS data and Euler poles. The authors defined their region by using existing GNSS continuous and episodic data, previous studies that show areas of rigidity, and derived seismicity information from the International Seismicity Catalog. Based on these data sets, they outlined zones of profuse seismicity along the EARS to define spatial extents of rigidity versus deformation where in zones of rigidity GNSS observation stations are not used in the model. It is for this reason that the authors used the Haines and Holt approach because it ensures a slow partial variation of the strain rates in deforming zones constrained by GNSS data. The authors found the highest strain rates localized along the Main Ethiopian Rift, near Rukwa rift at the Victoria-Nubia-Rovuma plates intersection, along the Tanganyika rift, and finally at the northern Malawi Rift. However, along the EARS, the Turkana Rift has significantly lower strain rates compared to the Magadi and

the southern Northern Tanzania Divergence, and the Natron Rift. However, this observation could have been due to the sparse GNSS observations in the area then. Additionally, the new strain rate model showed a general E-W extensional movement where deforming zones portrayed larger strain rates compared to low strain magnitudes in rigid interiors.

However, Knappe et al. (2020) did a research study in the Turkana Rift where there previously was poor GNSS observations, in NKR. They used GPS observations to study the extension and accommodation mechanisms along the EARS. They studied the Turkana profiles where extension was confined along narrow fault zones and volcanic centers, and found that this region portrays high localized strain rates during extension, unlike low strain rates in areas of elevated topography in the MER. They also found a decreasing extension velocity southward into the Turkana Depression, as expected for the Euler Pole at the south of the EARS, since tangential extensional velocities increase farther from the Euler pole (United States Naval Academy, 2022), with the north of Turkana Depression showing a 4.4 mm/yr eastward extensional velocity. Euler pole parameters, which are globally defined, quantify either relative or absolute plate geodetic motions (Aktuğ & Yildirim, 2013) through pole of rotation that cuts through the Earth's center. This is in line with the Euler theorem that states that any rigid body's motion on a sphere's surface can be appropriately represented as a rotation relative to the appropriate rotation Euler pole (Stein, n.d.). The authors also find the importance of GPE in extension rates in heterogeneous lands (lateral mechanical heterogeneity) since it influences the scale of active rifting. The authors claim that GPE gradients are related to Ethiopian Highlands' distributed deformation and rheology. Thus, where there is high topography with thick crust, stretching happens beyond the structural rifts, with the regions outside the rift accommodating as much extension as the rift, resulting to low strain rates. Therefore, based on this, the Turkana Depression's lack of topographic gradient predicts the localized extension since the area has a thin crust and the extension is accommodated by only a single structure, leading to localized high strain rates.

Even so, experts still argue on the causes of plate divergence. Despite the debates on what leads to plate divergence, mantle flow is believed to be a significant leading component, as mentioned by Ebinger (2005). Some claim that rifting is aided by basal shear tractions due to divergent mantle flow, while others claim the divergence is due to lateral GPE variations caused by the high East African topography, leading to tensional deviatoric stresses. Astoundingly, the

GPE variation seems to be supported by the existence of the African Superplume that leads to positive thermal buoyancy. Finally, others claim that the divergence is powered by friction on faults that oppose plate motion resistance. However, in their study, Stamps et al. (2015) concluded that buoyancy forces-associated torque balance in Africa's lithosphere, Couette-type mantle flow within sub-African asthenosphere, and weak continental faults, significantly contribute in the explanation of the Nubian and Somalian plates divergence. As a result, buoyancy due to GPE variations influenced by topography is sufficient to power divergence between the two plates across the EARS. Therefore, the topography variations (GPE) caused by the African Superplume are likely the primary driving divergence forces that lead to the dynamic Eastern Africa uplift.

This is in line with Rajaonarison et al. (2021) who agree there still are challenges in identifying the relative contributions of the forces driving continental drifting due to the complex lithospheric rheology that is nonlinear with a depth-dependent nature. Therefore, to identify crustal deformation styles, dynamic velocities, and continuous strain rates caused by lithospheric buoyancy-induced forces, the authors used ASPECT to model present-day model. GPS observations and azimuthal seismic anisotropy, and strike-slip mechanisms are used to compare with model output. The slip-free model on all sides except the fixed bottom side was used for surface deformation. Additionally, to find crustal density variations and assuming it being independent of temperature, the authors used CRUST1.0 and ETOPO1 in the model. Their simulated 3D thermomechanical EAR models showed that lithospheric buoyancy primary drives the E-W extension across the EARS, in line with Stamps et al. (2010, 2015). This lithospheric buoyancy is due to surface topography as influenced by vertical mantle flow and a combination of lithospheric structural changes; geothermal gradients and composition. As a result, lithospheric regions with locally high GPE tend to experience faster extension.

Lithospheric buoyancy is then the predominant force that drives the Nubian-Somalian divergence along the EAR in the E-W direction, while the African Superplume hypothetically leads to the northwards surface motions due to the north coupling mantle flow. Therefore, while the lithospheric buoyancy is basically in rigid plates, the viscous coupling to mantle flow may play a significant role in weak zones between continental blocks.

2.4 Vertical Displacement due to Rifting

Continental rifting is a complex evolutionary process that produces many geometrical features, including crustal subsidence. Corti et al. (2015) find that the resultant subsidence in rifting basins during continental extension is poorly understood. As a result, the authors modeled axial mafic intrusions from East Africa's MER and Afar Depression with the aim of understanding if these intrusions cause the opening rift's downward flexure. However, it is known that magma intrusion can accommodate high extension rates before the development of a new oceanic crust bounded by a young continental crust. This is because magma emplacement into the lithosphere is a slow process that significantly modifies the heat transfer rates to the plate and density profiles of the crust (Corti et al., 2015; Ebinger et al., 2013). The slow loading process in the axial rifts over a large time scale leads to significant surface and internal loading of the crust. Astoundingly, the authors found that loading induces a non-linear kind of subsidence in crustal axial rifts after continuous crustal thinning and heating. This is because of the weakening of the plate as the magmatic intrusions induce subsidence loading, a crucial evolution mechanism during rifting. They concluded that intrusion-related loading, like crustal magmatic intrusions, can cause 1 km (approximately 33%) of the entire subsidence during rifting. Therefore, large volumetric crustal intrusions significantly control rifting morphology over time.

Even so, understanding that there is limited knowledge about fault rifting and the length and time scales of magmatism associated with it, Pagli et al. (2015) set to present contributions of a variety of processes that occur during tectonic plates divergence. Acknowledging that lithospheric thinning due to mantle intrusion into the crust leading to ductile stretching occurs at depth while brittle crustal responses occur shallowly near the surface, the authors state that one of the geometries that come with continental rifting is crustal subsidence.

Therefore, the rifting process has many dynamics, with subsidence being one of its primary ones. Keen (1985) postulates that rifting dynamics may significantly modify a rift zones' uplift or subsidence. As a result, vertical changes are inevitable during continental extension. This is due to the upwelling of the mantle as the crust thins, leading to subsidence during initial isostatic adjustment as the hot asthenosphere replaces the cold lithosphere (Keen, 1985; Ebinger et al., 2013). However, the rate of subsidence decreases with time as the basins get wider and deeper.

However, the initial extent of the rift zone also affects the rate of subsidence during continental extension.

2.5 Vertical Displacement due to Continental Water Loading

While the phenomena of plate extension along the Kenyan Rift Valley is going on, another outstanding scientific problem of rising water levels is observed in the string of lakes along the Kenyan Rift System (Ministry of Environment and Forestry, 2022). This phenomenon of rising lake levels is important since it directly influences the population and the ecosystem biodiversity in the lakes' vicinity. According to Avery (2020), who, for decades, has worked on East African hydrology, the rising lake levels are worrying since by October 2020, more than 5,000 people had been displaced due to the rising waters of Lake Baringo only, a case also observed for Lake Nakuru and Bogoria. Avery keenly notes that the rising lake levels are directly associated with the recent above-average rainfall in the Rift Valley Basin, with the end of 2019 receiving more intense rainfall. While the lakes water cycles are governed by rainfall in the highland catchment areas, seepage and evaporation, rivers, direct rainfall into the lakes, groundwater flows, and springs in some instances contribute to water reaching lakes. This is in line with Muita et al. (2021) who claim that increased rainfall levels have been consistent with the rising lake levels. Avery further reports that since 1932, Lake Naivasha reached its highest in 2020 May. However, he mentions that this is not a new phenomenon since historically, other rift valley lakes have had higher levels. During the wetter Holocene period, the regional lake water levels were higher to the point that Lake Bogoria and Lake Baringo were merged, and Lake Turkana was 100 m higher than the present level. Additionally, Moore (2021) predicts that Turkana's river inflows will likely experience heavier rains in the coming years leading to future wetter periods.

The insights by Avery (2020) are also shared by Baraka (2022) who claims that the phenomenon of the rising lake levels along the rift valley was mistakenly discovered in 2013 by Simon Onywere, a geologist who was then studying if the fluoride levels in the waters of Lake Baringo adversely influenced the community's health due to their quick rate of bones becoming weak. Onywere, with the help of an old resident who brought up the concern, observed the severe damages that the rising lakes were causing like flooded schools and displaced people, making the resources unusable due to submergence, as Herrnegger et al. (2021) confirms, alongside adversely affecting biodiversity. For instance, in 2013, Lake Nakuru had increased by 50%. However,

Baraka (2022) attentively noted that there was an accelerated increase of the lakes at the start of 2020's viscous rainfall in the Kenyan highlands. While Lake Baringo started to rapidly increase in 2019, the residents hoped the risen levels would reside after the heavy downpour that went on for about three months up to March 2020. However, the level kept rising, leading to submergence of schools. While some consider such an occurrence a historical cyclic occurrence, some feel that the rising lake levels are due to the tectonic activities, and others due to an underground aquifer being brought close to the lakes, with some elders in El Molo theorizing broken springs or broken rocks that are transporting water into the lakes. However, the fact that Lake Victoria also recorded a huge increase in Lake water level and it is not along the Kenyan Rift Valley string of lakes led to Onywere disregarding the association of the tectonic activities and argued that the rise could be due to the ongoing climate crisis. This is based on the fact that the Kenyan and Ethiopian highlands have been experiencing more rainfall with the volume of the rivers feeding the lakes along the rift being high. This is astounding since in 2019, the rainfall experienced was the third highest ever recorded.

Understanding that crustal deformation can be caused by mass water loading, also known as continental water loading (CWL), Jiang et al. (2013) used different models to model the effect that various environmental loading phenomena have on International GNSS Service (IGS) reference stations. They used the Global Geophysical Fluid Center (GGFC), Loading Model of Quasi-Observation Combination Analysis software (QLM), and their self-modeled optimum model data (OMD) daily loading time series results models. The environmental loading effects modelled were changes caused by atmospheric pressure (ATML), continental water storage (CWS), and non-tidal ocean (NTOL) that induce displacement on a reprocessed time series sample of 233 global International GNSS Service (IGS) reference stations. These GNSS stations had more than 100 clean observations without offsets of more than two years. Following that Fritsche et al. (2012) had used 14 years of reprocessed GPS data from 208 global IGS stations to validate how CWS causes crustal deformation, the authors found that CWS temporal variations have capabilities to cause substantial vertical displacement variations.

With the knowledge that continuous GPS vertical component signals have been used in other global settings with robust periodic precipitation patterns like California, Argus et al. (2014) used GPS to track and assess typical temporal and spatial patterns and characterize large deviations

from typical water loading (Milliner et al., 2018). Birhanu & Bendick (2015) set to investigate the relationship between water load amplitude and crustal deflection amplitude in Ethiopia and Eritrea. Almost all of the continuous GPS station stations used for this study were on bedrock outcrops to avoid hydrological effects associated with aquifers. By applying a continuous GPS time series method from the GAMIT application, through cross-correlations, the authors compare their GPS vertical displacement time series solution to monthly precipitation time series and Gravity Recovery and Climate Experiment's (GRACE's) Liquid Water Equivalent Thickness (LWET). The recovered phase and magnitude by the continuous GPS stations showed measured vertical displacement where the stations moved geodetically down due to increased hydrological loading. The authors found that the vertical deflection amplitude from the GPS signal correlated to the monthly precipitation and LWET. The consistent observations between the GPS and GRACE's regional results further support the assumption that mass water loading, also known as continental water loading, can substantially cause vertical displacements. Astoundingly, the Afar region has a thicker lithosphere compared to Ethiopian Highlands and Somali Platform. However, the authors' resolution showed no relationship between the varying lithospheric thickness and flexural amplitude distribution. This means that the resulting solid Earth tides were in no way associated by the thinning lithosphere in the East African Rift. Thus, the authors concluded that mass water loading can deform East Africa's solid Earth.

Considering that continental water loading leads to seismicity, Birhanu et al. (2018) set to investigate seasonal deformation and seismicity patterns in the Aluto-Langano geothermal reservoir in Ethiopia. To study the seasonal seismicity variations, they used time series from four continuous GPS, twelve seismometers, and monthly lake level and precipitation data sets. Because GPS can be used to precisely measure seasonal vertical displacements caused by hydrological processes, they found that maximum lake loading was directly associated with primary seismic peak and subsidence. Therefore, with their GPS-derived ground-water storage estimates adequately corresponding to GRACE, the authors concluded that subsidence can be caused by surface loading.

CHAPTER 3: MATERIALS AND METHODS

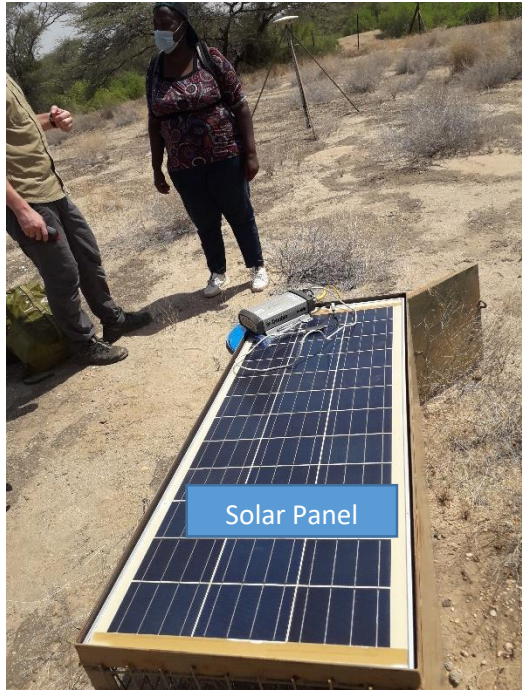
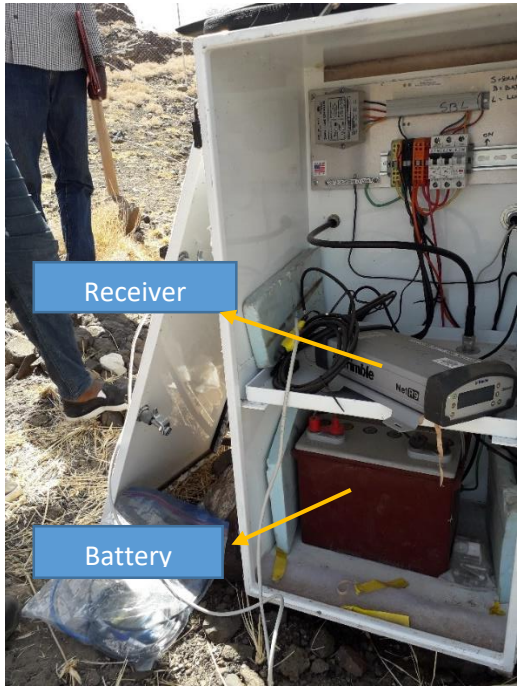
3. 1 Research Design

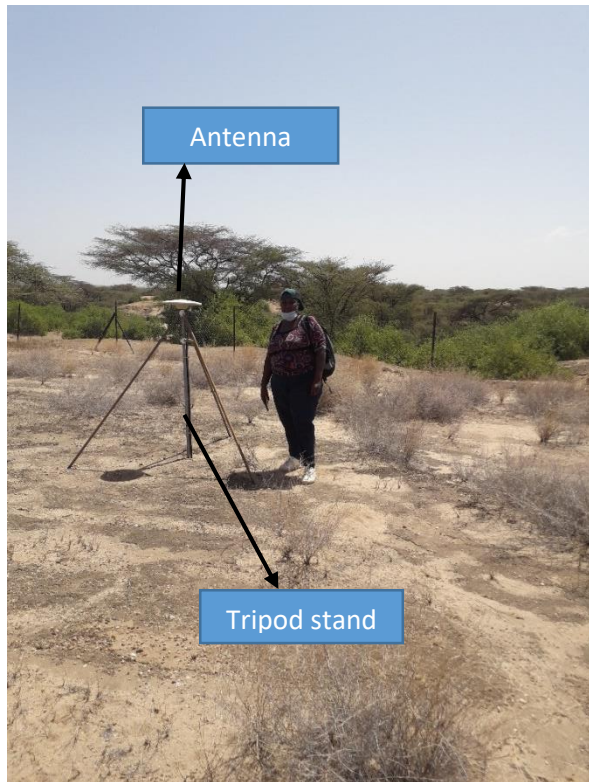
3.1.1 GNSS Data Collection

The research project involved acquisition of raw Receiver Independent Exchange (RINEX) data using dual frequency GPS receivers archived at UNAVCO (www.unavco.org). These dual frequency receivers recorded positions of steel masts anchored in bedrock in Earth. All the data were collected from thirteen high accuracy continuous permanent GNSS stations located in the NKR and CKR. The GNSS stations were roughly located along rift-normal lines with approximate spacing of 200 to 300 km between a pair of stations. As shown in the Figures 3.1 A, B, C and D below, a typical continuous GNSS station set up is composed of: a protected site, power supply, dual frequency GNSS receiver, a permanently mounted GNSS antenna on a stable bedrock/geodetic monument, continuous phase and pseudorange measurements at the rate of 30 seconds for 24 hours all year round, data collection approximately every 6 months, or as frequent as needed. Some of the essential ancillary equipment include; solar panels and power regulators, batteries, Ethernet cable, steel mast antenna mount anchored in bedrock, antenna cable, log sheets, compass, power cable, and appropriate documentation (Stamps, 2021). In this research project, the words site and station are used synonymously.

The raw data, as picked by the antenna, are sent to the dual frequency receiver in Binary Exchange (BINEX) format. However, these BINEX data go through preprocessing and conversion to RINEX format data before processing (Floyd & Herring, 2020).

Data Availability: The downloaded data was then uploaded to the Geodesy Data Facility UNAVCO online archive (www.unavco.org, doi:10.7283/T5SN077J, doi:10.7283/ T5WS8RKK, doi:10.7283/T5XD0ZZG) from where it was accessed for downloading. Appendix A gives a detailed GNSS data collection procedure.





C



D

Figure 3.1 A, B, and C showing a continuous station set-up. A shows the dual frequency receiver, and battery, B shows solar panels, C shows an antenna, and D shows a Beavis point driven into a stable bedrock, although our stations were steel masts anchored in bedrock.

Other than the acquired RINEX files from the project's thirteen GNSS stations, RINEX data from 26 more reference stations were downloaded from the UNAVCO online archive for processing. These reference stations were MAL2, ABPO, MBAR, REUN, VACS, DGAR, IISC, HYDE, BJCO, STHL, SUTM, HRAO, MAS1, LPAL, FUNC, SFER, NOT1, MATE, ZAMB, RAMO, NKLK, SUTH, WIND, DJIG, MTDK, ADIS.

3.1.2 Rainfall data for testing vertical displacement due to CWL

The meteorological factor that was considered for testing its impacts on crustal subsidence was rainfall. Gridded rainfall data used in this study were acquired from Kenya Meteorological Department (KMD) for nine meteorological stations namely: Ileret Police Station, Sibiloi Kokai Outpost, Eliye Springs Lodge, Green Hill Farm, Loieyangalani Police Post, Kibingor Primary School, Perkerra Agric Research St., Njoro Ogilgei Farm, and Menengai Farm, as shown in Figure 3.2. These rainfall stations were chosen on the basis that they were close to the GNSS stations near the four major lakes (Lake Turkana, Lake Baringo, Lake Bogoria, and Lake Nakuru) along the Kenyan Rift valley. Similar to the geodetic RINEX data, rainfall data from January 2017 to December 2021 were acquired for these rainfall stations for correlation purposes.

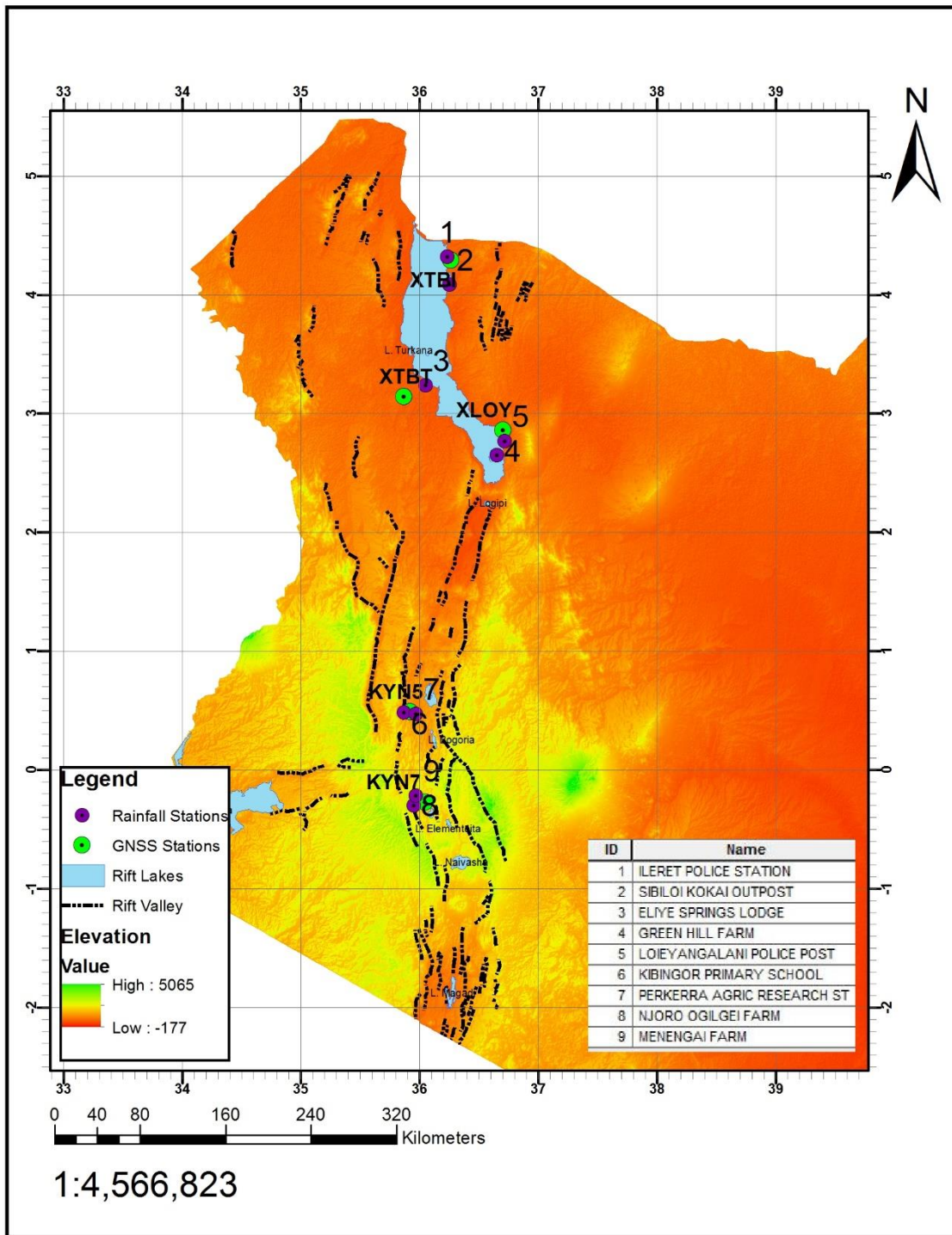


Figure 3.2 The GNSS stations, the Kenyan Rift Valley, the major lakes along the Rift Valley close to the GNSS stations, and the rainfall stations close to the GNSS stations,

3.2 Data Processing

The acquired RINEX binary data was processed using GAMIT/GLOBK (Herring et al., 2018), a desktop software developed by MIT, Scripps Institution of Oceanography, and Harvard University, and supported by the National Science Foundation. This processing was expected to provide precise velocity solutions to model the plate movements using Generic Mapping Tool alongside the time series from GAMIT/GLOBK. Using several commands, GAMIT/GLOBK was run in a chronological procedure as shown in Appendix B.

GAMIT loosely estimates satellite, atmospheric, orbital, phase parameters, and station coordinates from the raw observations. These estimates and their covariances are then combined with daily global solutions provided by MIT to generate position time series.

GLOBK uses outputs from GAMIT as its input and fits 14-day averages using a Kalman filter to estimate station velocities in the International Terrestrial Reference Frame (ITRF2014).

The GAMIT/GLOBK processing final velocities output was the `velocity_hz.psvelo` file.

3.3 Analysis

3.3.1 GAMIT/GLOBK Output Analysis for Velocity Break-up Rates and Trends

For GNSS output analysis, two programs were used; `rot` and `GMT`. The `rot` program makes it possible to place the velocity solutions in the desired reference frame. This is essential since the velocity output file from GAMIT/GLOBK processing was in the International Terrestrial Reference Frame. However, in this case the focus was on geodetic extension between the Victoria microplate and the Somalian plate. Therefore, the `velocity_hz.psvelo` file had to be placed in the right reference frame, which is the Nubia with respect to Victoria reference frame. `GMT` on the other hand uses, processes, and displays `xy` and `xyz` datasets in various forms of map projections. For this research project, `GMT` plotted the `velocity_hz.psvelo` file after placing it in the Nubia with respect to Victoria reference frame.

3.3.1.1 Rot

The `velocity_hz.psvelo` file created in the `vsoln` directory was used to answer the objectives on the Victoria microplate and Somalian plate velocity break-up rates and trends. To accurately do this, by looking at how the Victoria microplate is moving away from the Somalian plate, the velocities were placed in a Victoria with respect to (`wrt`) Nubia reference frame. To do this, the `rot`

program was used, starting with the `velocity_hz.psvelo` output file from GAMIT/GLOBK processing, which had the velocity solutions for all processed stations, including the reference stations. However, for an accurate break-up velocity plot, only stations with at least 2.5 years of processed data, as reflected in their time series, to account for seasonal signals were considered (Blewitt & Lavallée, 2002). The stations with at least 2.5 years of processing included XTBI, XTBT, KYN2, KYN3, KYN4, KYN6, KYN7, and MAL2. A detailed procedure on how to use the rot program to place velocity break-up rates in the Victoria-Nubia plate reference frame is given in Appendix C.

The final output from running the rot program to put the velocity break-up rates in Victoria with respect to (wrt) Nubia reference frame was `awk_nub_wrt_vic_keny.psvelo`.

3.3.1.2 PYGMT

To plot `awk_nub_wrt_vic_keny.psvelo` using GMT, the pyGMT terminal (in this case the Git Bash terminal) was used. The `awk_nub_wrt_vic_keny.psvelo` file was transferred from the remote gtl computer in the United States to pyGMT using the command

```
scp janewambui@gtl.geos.vt.edu:/home/janewambui/rot_files/awk_nub_wrt_vic_keny.psvelo .
```

However, in pyGMT, plots are made by running executable scripts. Therefore, an executable script for the horizontal displacements was created using the vi command in GMT for plotting the psvelo file as a vector map. The script used to create the vector maps is as shown below in figure 3.3. This script in pyGMT was called `plot_velocity_hz.sh`.

```
#!/bin/bash
# plotting horizontal and vertical velocities for GNNS kenya stations
# made by Jane on 27th July 2022
echo "scriptname inputfilename outputfilename"

J="-JMS.5i"
#define the projection. this applies to all scripts.
R="-R26/44/-6/8"
#define theh region. it begins with min long, max long, then min lat, max lat
B="-Ba2f2g2"
#define the border
input="$1"
#define the output file name
output="$2"
#define the output name
format="jpg"
#define output format

gmt begin $output $format

gmt basemap $J $R $B
#generate a basemap
gmt coast $J $R -W0.5,blue -Sskyblue -Df -A100 -N1/0.5p,black
#water body definition of borderlines
gmt velo $1 $R $J -W1.0p,black -Gblack -Se0.1/0.95/5 -A0.2c+p0.1p+e+gred
#plotting horizontal psvelo velocities
echo "30 7 10 0 0 0 horizontal velocities 10 mm/yr" | gmt velo $R $J -W0.5p,black -Gblack -Se0.1/0.95/5 -A0.2c+p0.5p+e+gred
gmt end show
~
~
```

Figure 3.3 The plot_velocity_hz.sh script

To execute this shell script and plot it to have a visual on the modelled velocities, the command `./plot_velocity_hz.sh awk_nub_wrt_vic_keny.psvelo awk_nub_wrt_vic_keny.psvelo` was used.

3.3.2 Calculating for GPE as Influenced by Topography

To determine the GPE variations between the NKR and the CKR, equation 3.1 was used.

$$GPE = Mass \times Height \times Gravitational\ Field\ Strength \text{ (HyperPhysics, 2016)} \quad \dots\dots Eq:3.1$$

However:

$$Mass = Volume \times Density \quad \dots\dots\dots Eq:3.2$$

$$\text{While } Volume = Area \times Thickness \quad \dots\dots\dots Eq:3.3$$

The crustal thicknesses used for NKR and CKR were 20km and 35km respectively, according to Chorowicz (2005). Additionally, the standard crustal density used for this calculation was $2.64 \times 10^3 \text{ kg m}^{-3}$, according to Henry et al. (1990), while the standard Earth's gravitational pull applied was the prior calculated 9.81 m/s^2 , according to Jöriges & López-Moliner (2020). To find the area of the regions, Geographic Information System (GIS) was used.

3.3.3 Vertical Displacement due to CWL Analysis

For CWL-induced vertical displacement analysis to observe crustal subsidence, two programs were used; tsview, and Microsoft Excel 2013. MATLAB was exploited by installing tsview and running it in the software. Tsview makes it possible for one to run tests for vertical displacements in a visual manner. This software made it possible to test and identify if there were semi-annual, annual, or both annual and semi-annual signals in the vertical displacement by observing the WRMS (weighted root mean square). This is founded on the fact that tsview determines the best fit line by considering the rate, with or without seasonal signal. Therefore, by applying both annual and semiannual signals that fit the model well, then there will be proof of seasonality. On the other hand, Microsoft Excel creates time series of variables that continuously vary over time. It thus helped to identify how the vertical displacement (the height variable) changed over time from plotting data found in station position time series files for the stations close to the lakes (XTBI, XTBT, XLOY, KYN5, and KYN7).

3.3.2.1 Tsview Analysis of Station Position Time Series files

In this software, the station position time series files (`sh_plot_pos -f *.pos`) from prior GAMIT/GLOBK processing for five GNSS stations namely XLOY, XTBI, and XTBT, KYN5 and KYN7 were processed. These GNSS stations were chosen on the basis that they were close to the major lakes along the EARS in Kenya. The command `scp janewambui@gtl.geos.vt.edu:/home/janewambui/keny/vsoln/KYN7.gtl.final_igs14.pos .` was used to copy the `sh_plot_pos -f *.pos` files from the remote gtl computer in the United States to the local terminal. The `sh_plot_pos -f *.pos` files were then transferred to the desktop using the command `cp KYN7.gtl.final_igs14.pos /mnt/c/Users/user/Desktop/`. Appendix D shows how to check for seasonality with tsview.

It was made sure that the station position time series files for these five stations were inside the tsview folder for readability. Once the station position time series files were readable in tsview, by clicking on one file for a specific station since the program analyzes one set of data at a time (a process that was followed through with the other files too), the load button was clicked on the interface to load the selected station's data.

The values acquired from running tsview, as shown in table 3.1, included Weighted Root Mean Square (WRMS), an attribute that is crucial in observing seasonality in data.

Table 3.1 Showing a tabulated data for the values that processing with tsview provides for GNSS station XLOY, including the crucial WRMS

XLOY									
Detrend of XLOY.gtl.final_igs14 Up									
NO SIGNAL								ERROR	UNIT
WRMS:	4.21mm		NRMS:	1.7		#: 233 data			
Mean						0.1	0.63	mm	
Rate						-15.32	1.18	mm/yr	
ANNUAL SIGNAL									
WRMS:	4.15mm		NRMS:	1.61		#: 233 data			
Mean						-0.13	0.62	mm	
Rate						-15.34	1.2	mm/yr	
Annual Cos						-0.86	0.87	mm	
Annual Sin						-0.86	0.92	mm	
SEMIANNUAL SIGNAL									
WRMS:	3.83mm		NRMS:	1.24		#: 233 data			
Mean						0.16	0.46	mm	
Rate						-15.12	0.86	mm/yr	
SemiAnnual Cos						-1.5	0.65	mm	
Semi Annual Sin						2.01	0.66	mm	
ANNUAL AND SEMIANNUAL									
WRMS:	3.79mm		NRMS:	1.18		#: 233 data			
Mean						-0.01	0.46	mm	
Rate						-14.88	0.89	mm/yr	
Annual Cos						-0.94	0.65	mm	
Annual Sin						-0.19	0.69	mm	
SemiAnnual Cos						-1.6	0.63	mm	
SemiAnnual Sin						1.89	0.65	mm	

The primary observations needed were the rate to see which data gives the best fit, and the WRMS values for the varying signals.

3.3.2.2 Analysis of rainfall data using Microsoft Excel 2013

To check for the seasonality in rainfall data, Microsoft Excel 2013 was used to create a time series of the data. Additionally, Microsoft Excel 2013 was exploited to plot time against the varying height components in the station position time series files that are highlighted in table 3.2. This is because the station position time series files have multiple station positioning information and how they vary with time. One of these primary changing components is height, an essential component that shows how the Earth's crust moves over time.

Table 3.2 Showing an excel sheet derived from a Station Position Time Series file data highlighting the time and height values

1	2	3	4	5	6	7	8	9	10	11	12	13	14	15	16	17	18	19	20	21	22	23
****MM/HHMMSS	HHMMSS	UUUUUU	X	Y	Z	Z-variables	Sx	Sy	Sz	Rvx	Rvz	Nlat	Elong	Height	dn	de						
20180214	115900	58169.5	5128869	3762318	473501.125560	0.125560	0.00503	0.0041	0.00149	0.861	0.294	0.278	4.285828	36.26217	424.7539	-0.02383	-0.03731					
20180217	115900	58166.5	5128869	3762318	473501.124260	0.124260	0.00404	0.00325	0.00119	0.863	0.274	0.252	4.285828	36.26217	424.759	-0.02552	-0.03649					
20180220	115900	58169.5	5128869	3762318	473501.124510	0.124510	0.00462	0.00371	0.00135	0.861	0.281	0.259	4.285828	36.26217	424.7626	-0.02555	-0.03571					
20180223	115900	58172.5	5128869	3762318	473501.123540	0.123540	0.00453	0.00364	0.00133	0.862	0.282	0.258	4.285828	36.26217	424.7602	-0.02634	-0.03527					
20180226	115900	58175.5	5128869	3762318	473501.124290	0.124290	0.00512	0.00408	0.0015	0.866	0.304	0.285	4.285828	36.26217	424.7551	-0.0252	-0.03523					
20180301	115900	58178.5	5128869	3762318	473501.124280	0.124280	0.00461	0.00367	0.00136	0.866	0.309	0.288	4.285828	36.26217	424.7549	-0.0252	-0.03447					
20180304	115900	58181.5	5128869	3762318	473501.122870	0.122870	0.00377	0.003	0.0011	0.868	0.292	0.278	4.285828	36.26217	424.7539	-0.02654	-0.03507					
20180307	115900	58184.5	5128869	3762318	473501.124720	0.124720	0.00475	0.0038	0.00136	0.866	0.305	0.282	4.285828	36.26217	424.7559	-0.02483	-0.03496					
20180310	115900	58187.5	5128869	3762318	473501.124370	0.124370	0.00374	0.00305	0.00108	0.855	0.291	0.264	4.285828	36.26217	424.7564	-0.02522	-0.03465					
20180313	115900	58190.5	5128869	3762318	473501.124970	0.124970	0.00412	0.00328	0.00118	0.869	0.27	0.243	4.285828	36.26217	424.7586	-0.02478	-0.03428					
20180316	115900	58193.5	5128869	3762318	473501.126510	0.126510	0.00414	0.00329	0.00119	0.862	0.288	0.254	4.285828	36.26217	424.7594	-0.02329	-0.03409					
20180319	115900	58196.5	5128869	3762318	473501.125730	0.125730	0.00472	0.00377	0.00132	0.862	0.292	0.262	4.285828	36.26217	424.7608	-0.02417	-0.03391					
20180322	115900	58199.5	5128869	3762318	473501.125020	0.125020	0.00494	0.00382	0.00141	0.867	0.303	0.273	4.285828	36.26217	424.7505	-0.02411	-0.03596					
20180325	115900	58202.5	5128869	3762318	473501.124870	0.124870	0.00386	0.00306	0.00114	0.855	0.252	0.232	4.285828	36.26217	424.7553	-0.02463	-0.03371					
20180328	115900	58205.5	5128869	3762318	473501.125020	0.125020	0.00356	0.00283	0.00103	0.859	0.251	0.221	4.285828	36.26217	424.7583	-0.02433	-0.03295					
20180331	115900	58208.5	5128869	3762318	473501.125370	0.125370	0.00373	0.00293	0.00109	0.854	0.253	0.231	4.285828	36.26217	424.7571	-0.02426	-0.03343					
20180403	115900	58211.5	5128869	3762318	473501.125580	0.125580	0.00413	0.00325	0.00121	0.859	0.249	0.222	4.285828	36.26217	424.7583	-0.02414	-0.03445					
20180406	115900	58214.5	5128869	3762318	473501.125080	0.125080	0.00475	0.00369	0.00114	0.857	0.267	0.229	4.285828	36.26217	424.7547	-0.02437	-0.03346					
20180409	115900	58217.5	5128869	3762318	473501.126420	0.126420	0.00445	0.00352	0.00127	0.862	0.273	0.225	4.285828	36.26217	424.7527	-0.02288	-0.03286					
20180412	115900	58220.5	5128869	3762318	473501.125130	0.125130	0.00372	0.00292	0.00107	0.856	0.259	0.235	4.285828	36.26217	424.7494	-0.02392	-0.0326					
20180415	115900	58223.5	5128869	3762318	473501.125710	0.125710	0.00363	0.0029	0.00106	0.854	0.265	0.251	4.285828	36.26217	424.7564	-0.02386	-0.03297					
20180418	115900	58226.5	5128869	3762318	473501.125300	0.125300	0.0035	0.00277	0.00101	0.854	0.238	0.217	4.285828	36.26217	424.7497	-0.02377	-0.03343					

CHAPTER 4: RESULTS AND DISCUSSION

4.1 Results

4.1.1 Velocity Break-Up Rates and Trends Along the Kenyan Rift between the Victoria Microplate and the Somalian Plate

Data in psvelo files are arranged in columns that define them, as shown in table 4.1. There are seven columns in total and from the left their definitions are: longitude, latitude, velocity east (Ve), velocity north (Vn), sigma east (σ_e), sigma north (σ_n), and correlations.

Table 4.1 The definition of data in a psvelo file (in this case, the awk_nub_wrt_vic_keny.psvelo file)

LONGITUDE	LATITUDE	Ve	Vn	σ_e	σ_n	CORRELATIONS	SITES (~2.5 YRS)
35.86686	3.13934	-1.41	1.58	0.05	0.04	-0.01	XTBT_GPS
36.26217	4.28583	0.5	-0.68	0.08	0.07	-0.004	XTBI_GPS
37.59223	0.27135	1.84	-0.9	0.09	0.08	-0.003	KYN2_GPS
38.52655	0.53474	2.81	-0.9	0.1	0.08	0.017	KYN3_GPS
36.55498	1.21228	1.28	-0.77	0.11	0.09	0.017	KYN4_GPS
35.34376	1.39053	-1.4	-1	0.19	0.17	0.083	KYN6_GPS
36.04422	-0.2732	0.63	3.24	0.2	0.17	-0.066	KYN7_GPS
40.19415	-2.99605	1.73	-1.41	0.07	0.06	-0.002	MAL2_3PS*

From the [awk_nub_wrt_vic_keny.psvelo](#) file created in the rot directory, the Ve and the Vn were used to find the extension rates of the Kenyan Rift Valley on the GNSS stations. The formula used to calculate for the velocity break-up rates was:

$$Magnitude = \sqrt{Vn^2 + Ve^2} \dots\dots\dots Eq:4.1$$

*Magnitude is the velocity break up rate.

Table 4.2 Calculations from V_e and the V_n to find velocity break-up rates along the Kenyan Rift Valley in the GNSS stations

SITES	V_e	V_n	$V_e.sq$	$V_n.sq$	$V_e.sq + V_n.sq$	$\sqrt{V_e.sq+V_n.sq}$
XTBT	-1.41	1.58	1.9881	2.4964	4.4845	2.117663807
XTBI	0.5	-0.68	0.25	0.4624	0.7124	0.844037914
KYN2	1.84	-0.9	3.3856	0.81	4.1956	2.048316382
KYN3	2.81	-0.9	7.8961	0.81	8.7061	2.950610106
KYN4	1.28	-0.77	1.6384	0.5929	2.2313	1.493753661
KYN6	-1.4	-1	1.96	1	2.96	1.720465053
KYN7	0.63	3.24	0.3969	10.4976	10.8945	3.300681748
MAL2	1.73	-1.41	2.9929	1.9881	4.981	2.231815405

By observing the GNSS stations according to how they are spatially distributed along the Kenyan Rift System from North (top) to South (bottom), as presented in table 4.3 below, the velocity break-up rates show a trend of varying extension rates between the NKR and the CKR. Appendix E shows the calculation of the errors for the velocity break-up rates.

*While the GNSS station MAL2 appears in tables 4.1 and 4.2, its velocity break-up rate does not appear in table 4.3 because it was reference station in Kenya but not one of the project's GNSS stations. Therefore, it was excluded from table 4.3, which only lists the GNSS stations. Additionally, the naming of the GNSS stations in table 4.1 differ from the naming in table 4.2. This difference is because the three-character extension after the station names in table 4.1 is automatically generated by GAMIT/GLOBK as an identification after processing but the station four-character identification names are the given names of the GNSS stations.

Table 4.3 Velocity break-up rates for the GNSS stations along the Kenyan Rift Valley with the section on the left showing the velocity break-up rates as spatially distributed along the Kenyan Rift Valley with the section on the right showing the velocity break-up rates with the spatial distribution defined by the deformation and rigid zones

SITES	VELOCITIES	ERRORS	DEFORMING ZONE SITES	RIGID ZONE SITES
XTBI	0.8 mm/yr	±0.1	XTBI - 0.8 mm/yr	KYN3 – 3.0 mm/yr
XTBT	2.1 mm/yr	±0.1	XTBT – 2.1 mm/yr	KYN2 – 2.0 mm/yr
KYN6	1.7 mm/yr	±0.1	KYN6 – 1.7 mm/yr	
KYN4	1.5 mm/yr	±0.1	KYN4 – 1.5 mm/yr	
KYN3	3.0 mm/yr	±0.3	KYN7 – 3.3 mm/yr	
KYN2	2.0 mm/yr	±0.3		
KYN7	3.3 mm/yr	±0.1		

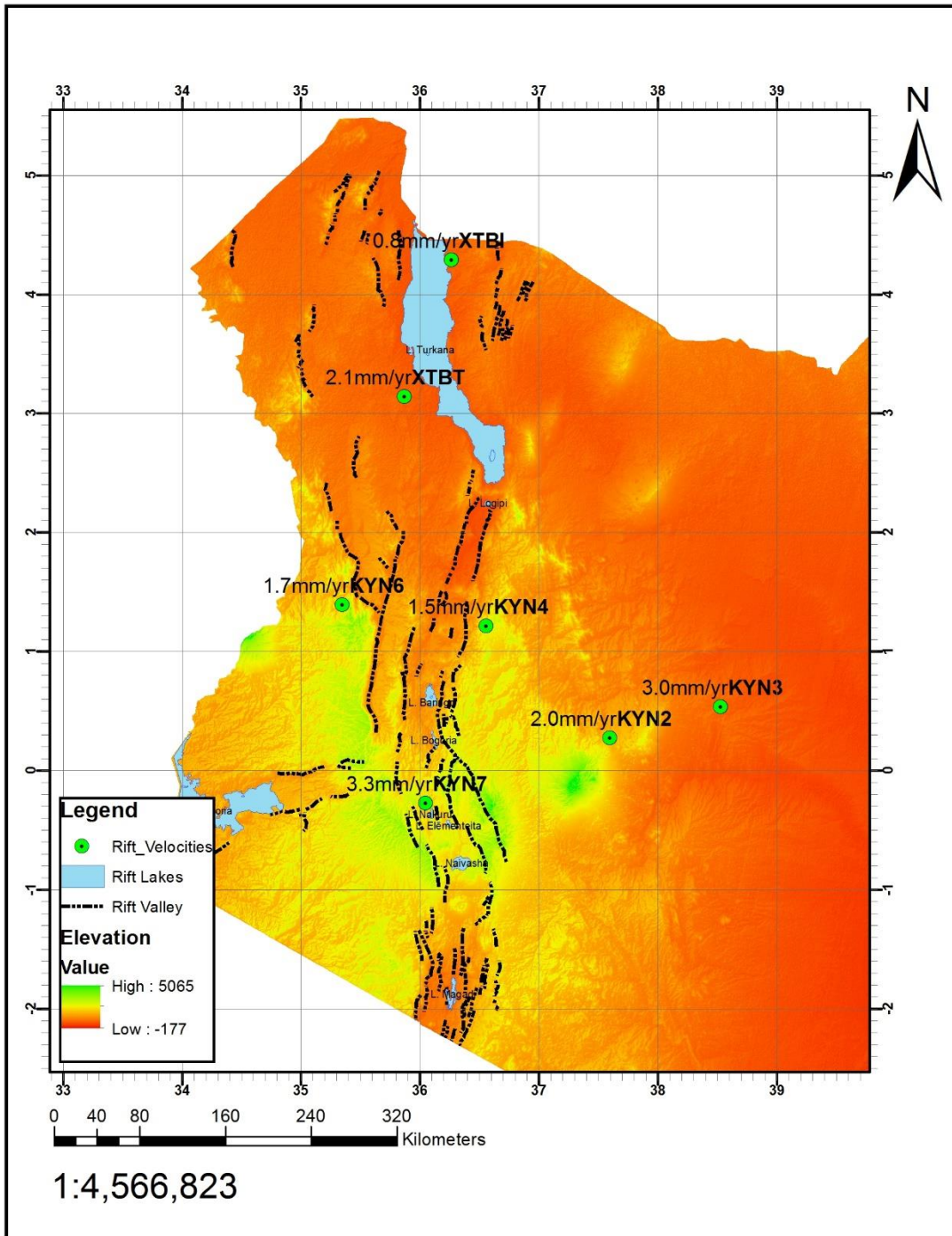


Figure 4.1 Velocity break-up rates for the spatially distributed GNSS stations along the Kenyan Rift Valley System

Additionally, after running the command `./plot_velocity_hz.sh awk_nub_wrt_vic_keny.psvelo awk_nub_wrt_vic_keny.psvelo` in pyGMT, the `awk_nub_wrt_vic_keny.psvelo.jpg` map output was as shown below in figure 4.2.

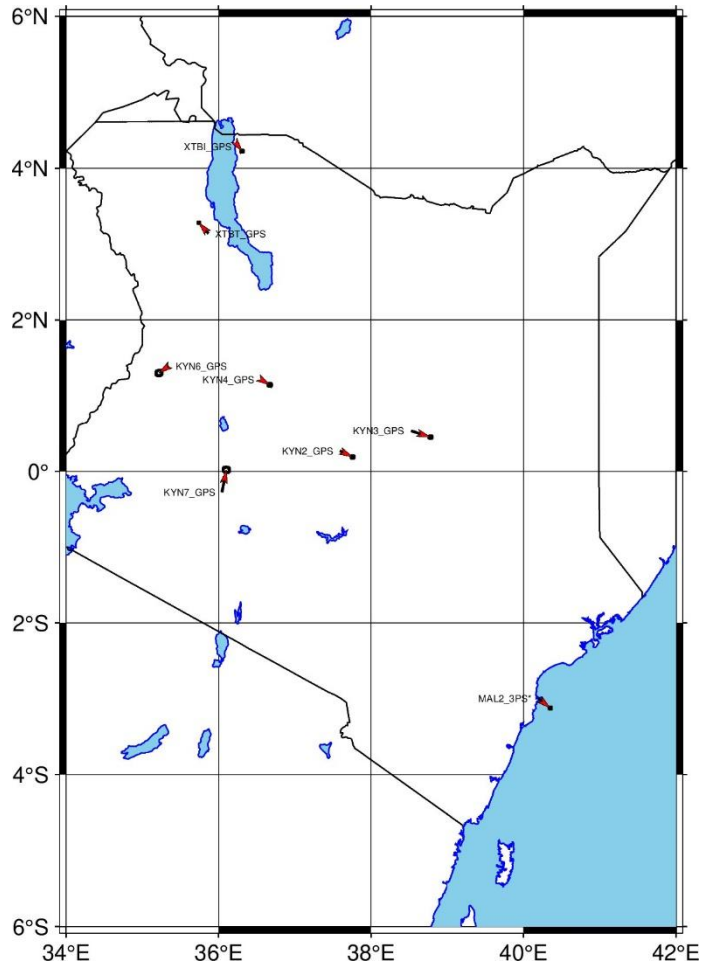


Figure 4.2 The extension trends as reflected by the GNSS stations along the Kenyan Rift Valley in a Nubia with respect to Victoria reference frame

4.1.2 GPE Influence on Velocity Break-Up Rates

The areas of NKR and CKR as determined by GIS were found to be 155241868084.53 m² and 172607473103.84 m² respectively. The following equations; $Volume = Area \times Thickness$, $Mass = Volume \times Density$, and $GPE = Mass \times Height \times Gravitational\ Field\ Strength$, as stated in section 3.3.2, were used to calculate GPE.

Therefore:

$$GPE = Area \times Thickness^2 \times Density^2 \times Gravitational\ Field\ Strength \quad \dots Eq:4.2$$

Using Density as $2.64 \times 10^3 \text{ kgm}^{-3}$ and the gravitational field strength as 9.81 ms^{-1} ;

$$GPE \text{ in NKR} = 155241868084.53 \times 20,000^2 \times 2640^2 \times 9.81 = 4.25 \times 10^{27} \text{ Joules}$$

$$GPE \text{ in CKR} = 172607473103.84 \times 35,000^2 \times 2640^2 \times 9.81 = 1.45 \times 10^{28} \text{ Joules}$$

4.1.3 Continental Water Loading and Crustal Subsidence

After plotting each station's four signals against their output WRMS from station position time series file using values from tsview, the varying WRMS values could be studied. WRMS is statistically used in measuring varying magnitudes.

Table 4.4 The WRMS for both annual and semiannual signals recorded the lowest values in tsview (signal 1 represents no signal, 2 represents annual signal, 3 represents semiannual signal, and 4 represents both annual and semiannual signals)

SIGNAL	WRMS				
	XLOY	XTBI	XTBT	KYN5	KYN7
1	4.21	5.28	3.98	6.3	5.27
2	4.15	4.34	3.57	5.69	5.31
3	3.83	5.13	3.66	5.7	5.44
4	3.79	4.12	3.08	4.88	4.95

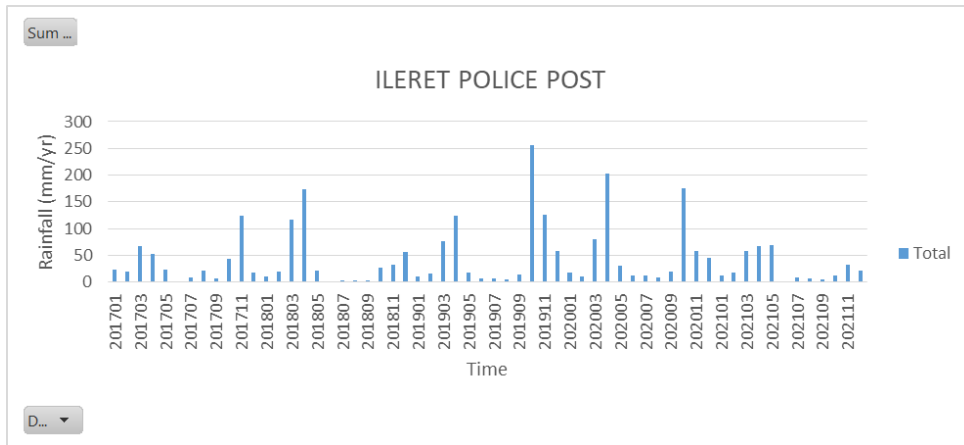
From these obtained outputs, the WRMS was lower in all the sites' data when processing both annual and semiannual signals, as presented in table 4.4 above. This shows that there is seasonality in vertical displacement for both annual and semiannual signals.

After plotting rainfall gridded data for locations close to the GNSS sites in Microsoft Excel 2013 to check for the seasonality in the data, time series showing the varying seasonalities were observed.

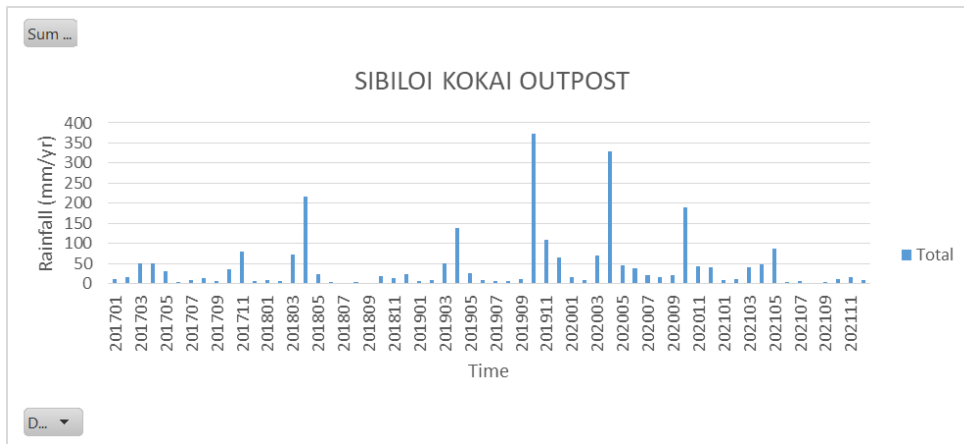
Additionally, after plotting time against the varying height components in the station position time series files, time series were also acquired.

The gridded rainfall data was compared to the varying height component data to see if there was an inverse correlation; a period of increase in rainfall correlates to a period of observed crustal subsidence, and a period of little or no rainfall correlates to a period of upward crustal flexure. Astoundingly, as expected, there was an observed inverse correlation for all sites where a period with increased rainfall reflected geodetic subsidence, and a period with little to no rainfall reflected increase in upward crustal amplitude.

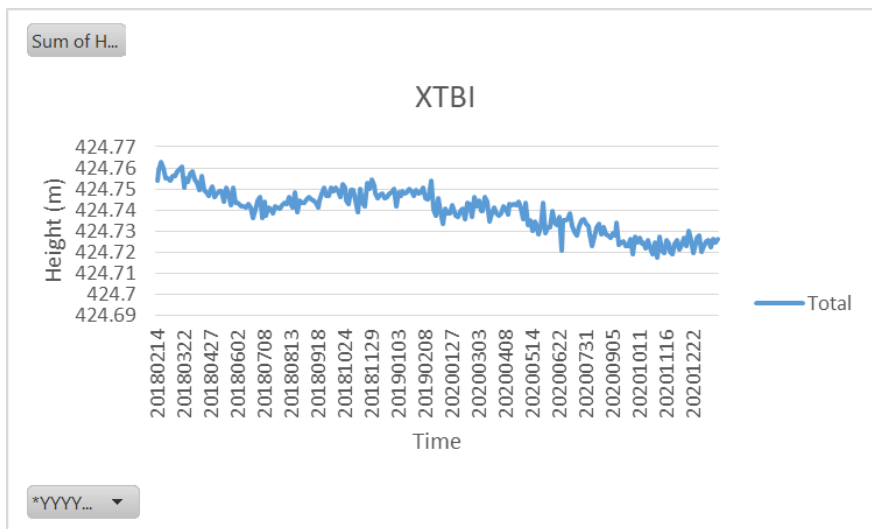
XTBI



A



B



C

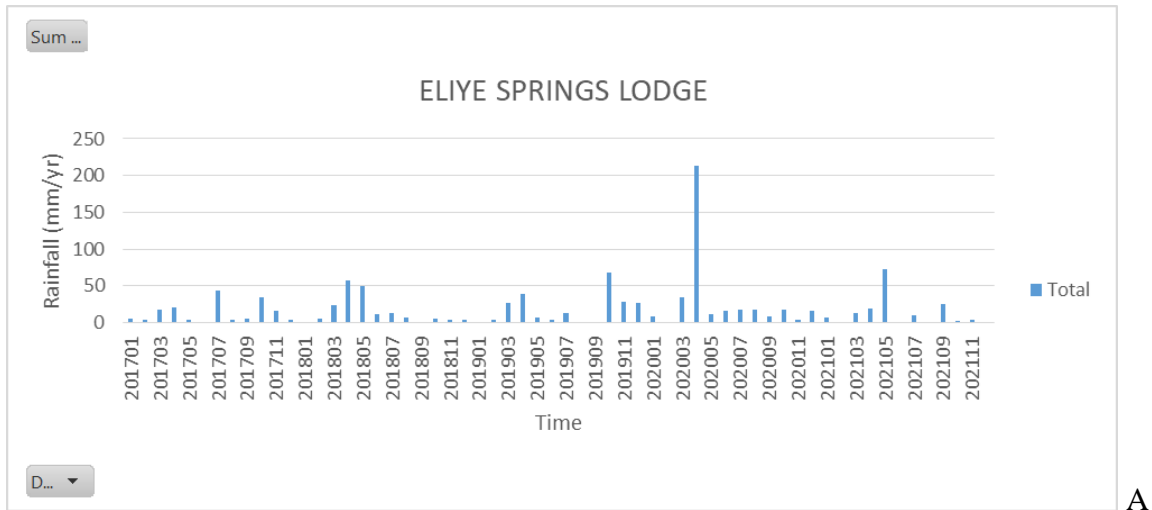
Figure 4.3 A and B showing rainfall in mm/yr against time for locations close to XTBI GNSS station while C shows XTBI's position estimate time series height in meters against time

The start of rainfall increase in 2018 March with a peak at April correlates to XTBI's continuous subsidence till 2018 June when the two rainfall sites experienced rain close to 0 mm/yr. Around 2020 July, there was a significant subsidence. This comes after the high rains in 2020 April of approximately 330 mm/yr in Sibiloi that resided in June 2020 at about 50 mm/yr and 200 mm/yr in Ileret Police Post. This shows a delay in subsidence as the water continuously accumulated leading to continental water loading. High 2020 October rains of about 190 mm/yr in Sibiloi and 170 mm/yr in Ileret Police Post also led to a maximum crustal subsidence in 2020 4th November of 424.7177 m.

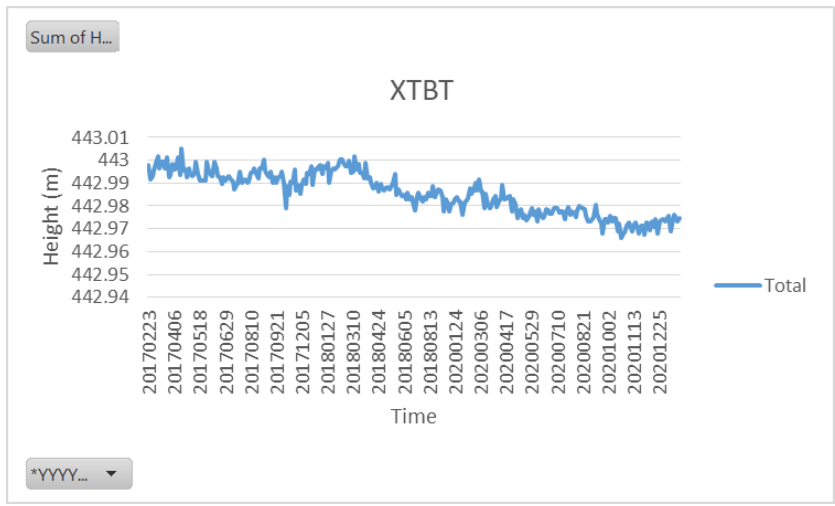
However, maximum upward vertical displacement of 424.7608 m was observed in 2018 19th March due to little rainfall from the previous months from 2017 December to 2018 February. There is also a significant upward amplitude in crustal displacements in 2019 February possibly related to the long dry season that lasted from 2018 May to 2019 February. There was also an observed continuous upward crustal movement from 2018 July to 2018 September due to little to no rainfall as shown by both Sibiloi Kokai Outpost and Ileret Police Post.

There was a difference of 0.0431 m vertical amplitude.

XTBT



A



B

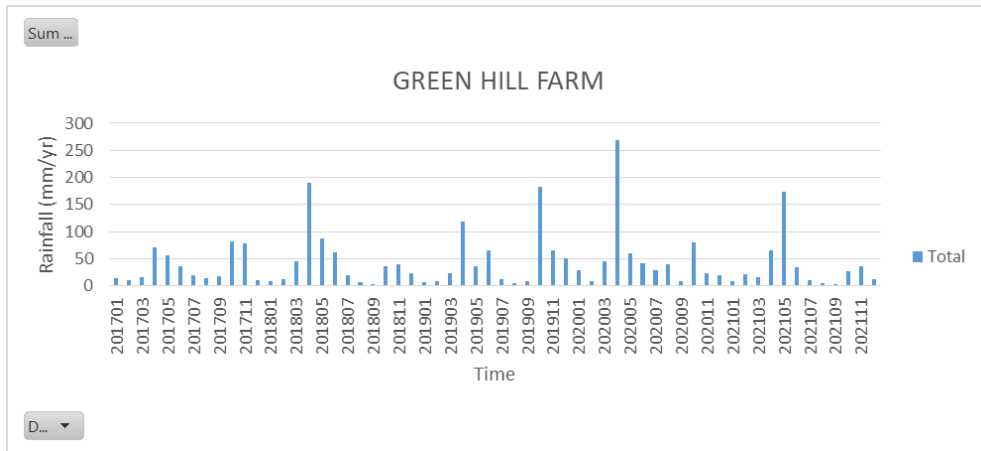
Figure 4.4 A showing rainfall in mm/yr against time for location close to XTBT GNSS station while B shows XTBT's position estimate time series height in meters against time

There is a significant observed subsidence at XTBT in 2017 October after low rainfall of about 40mm/yr that succeeded a dry season of very little rainfall in the Eliye Springs Lodge rainfall station. There was also another significant subsidence in 2020 May possibly linked to the high rainfall of 2020 April of about 210mm/yr. These observations portray an approximate one month of delay in subsidence due to water loading. After this there was a gentle continuous subsidence to a maximum of 442.9658m on 23rd October of 2020 due to the continuous low rains that continuously added weight to the crust over time.

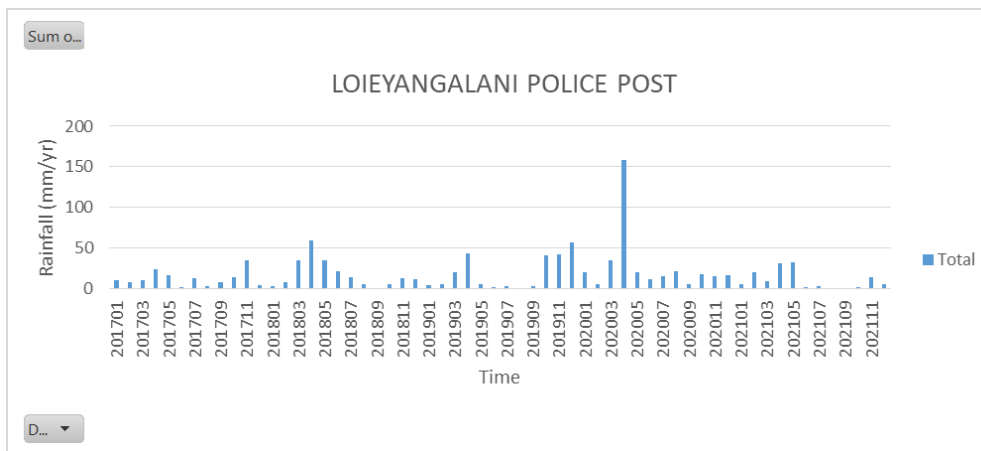
However, 2017 18th April experienced a maximum crustal upwarping of 443.0052 m possibly due to very little rainfall. A continuous upward crustal displacement from 2017 December to around 2018 February also correlates to very little rainfall, close to 0 mm/yr at Eliye Springs Lodge station.

There was a difference of 0.0394 m vertical amplitude.

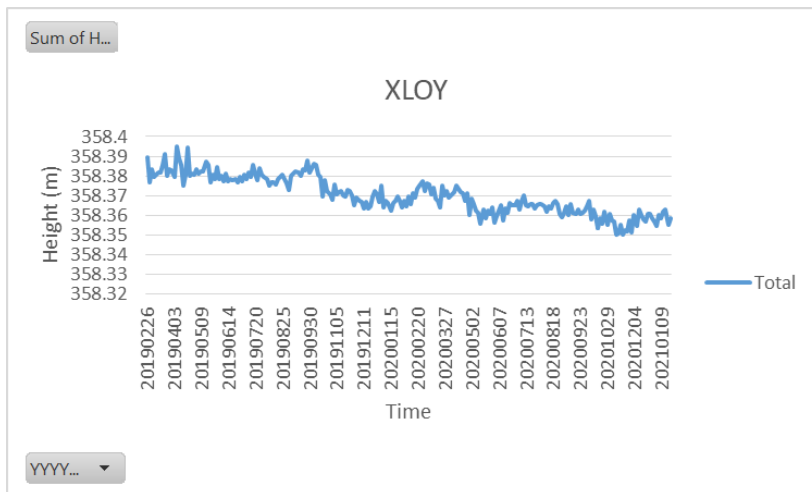
XLOY



A



B



C

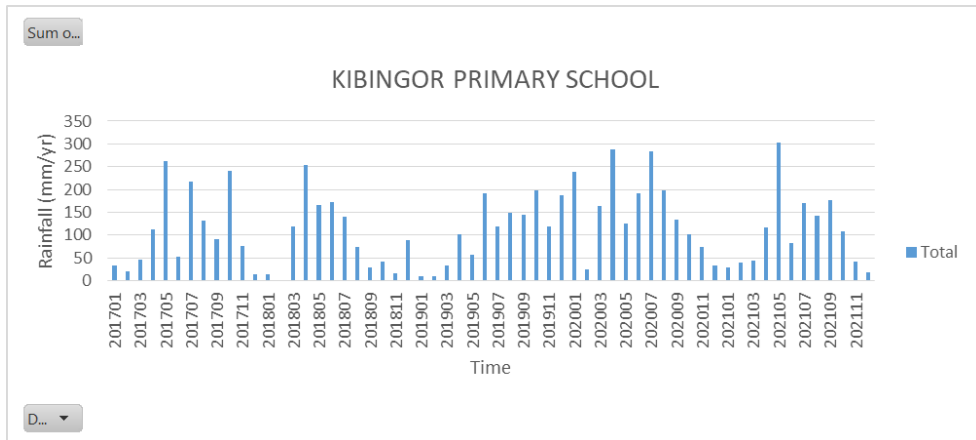
Figure 4.5 A and B showing rainfall in mm/yr against time for locations close to XLOY GNSS station while C shows XLOY's position estimate time series height in meters against time

There was an observed significant subsidence at XLOY in 2019 April that correlated with the rains in both Green Hill Farm of about 120 mm/yr and Loieyangalani Police Post of about 40mm/yr in that month after a dry season. 2020 May also experienced a significant subsidence that occurred after a high rainfall period in 2020 April of 270mm/yr in Green Hill Farm and 160 mm/yr in Loieyangalani Police Post. In between the rainfall and the observed crustal subsidence, there is approximately a one month delay in the subsidence. There was also a maximum subsidence of 358.35 m on 11th November 2020 at XLOY. This outcome was probably caused by continuous continental water loading due to low rainfall levels that persisted from 2020 May to 2020 December.

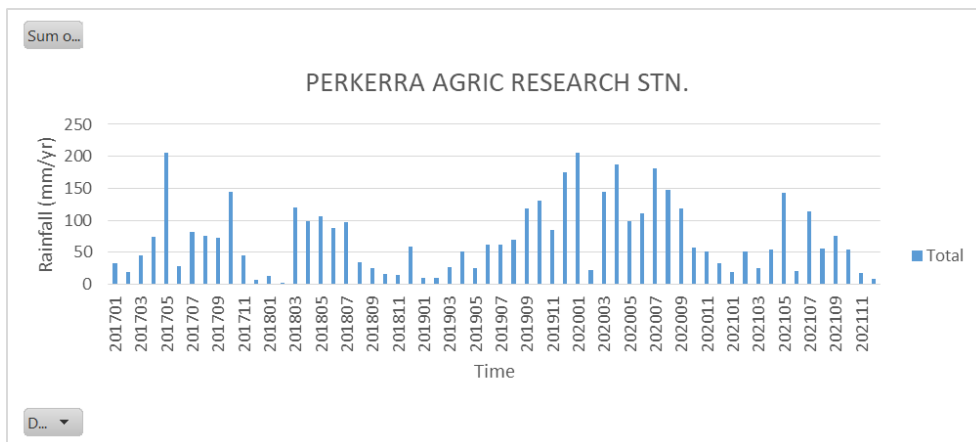
There was also a maximum upwards vertical amplitude to 358.39 m seen from 6th to 12th April 2019 due to the persistent dry season of low rainfall from 2018 August. However, since in 2018 April there was moderate rainfall of app 70 mm/yr in Loieyangalani Police Post and about 190mm/yr in Green Hill Farm, this maximum crustal upwarp was succeeded by a sudden subsidence. In 2019 September there was also an upward crustal displacement likely due to very little rainfall as seen in both rainfall stations.

There was a difference of 0.04 m vertical amplitude.

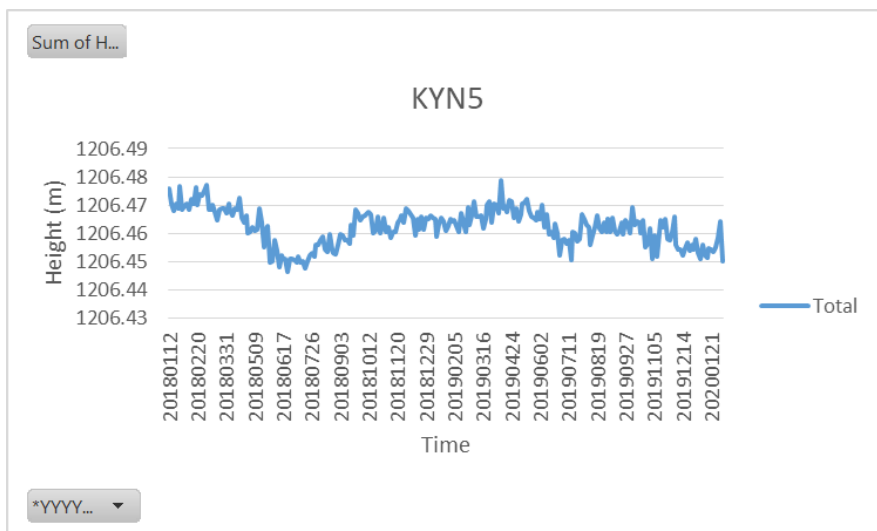
KYN5



A



B



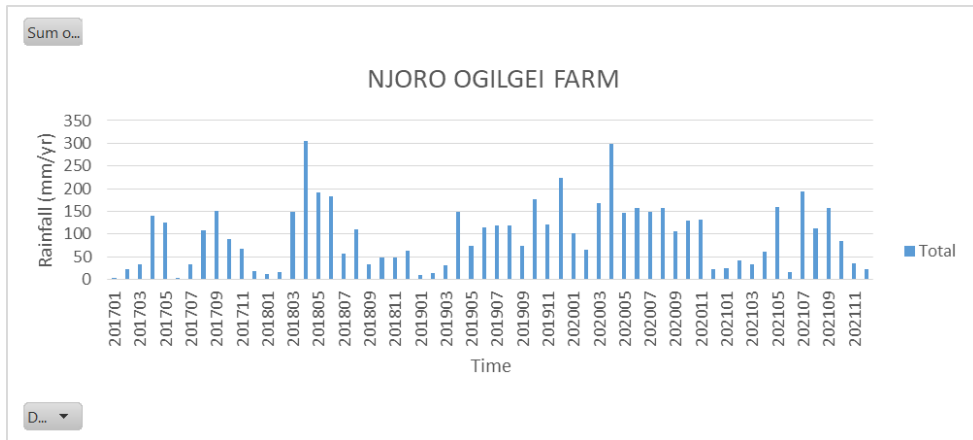
C

Figure 4.6 A and B showing rainfall in mm/yr against time for locations close to KYN5 GNSS station while C shows KYN5's position estimate time series height in meters against time

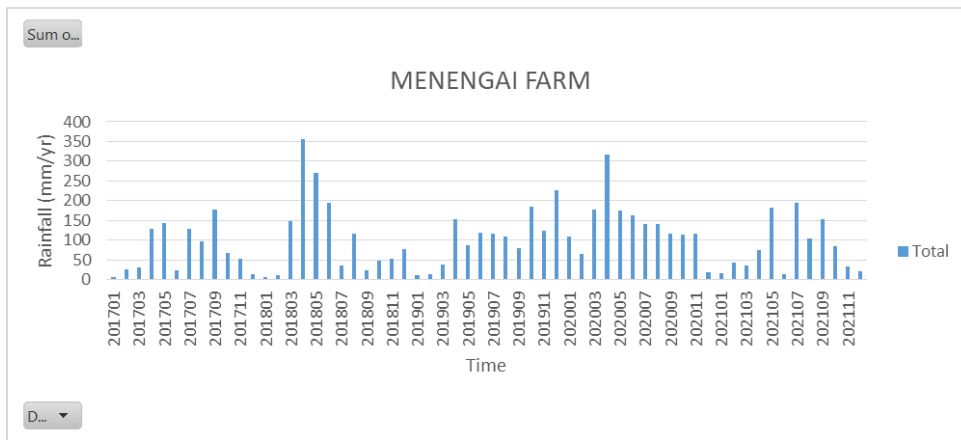
The rainfall stations close to KYN5 received generous rainfall from 2017 to 2021, with very few months of little rainfall. Maximum subsidence at 1206.446 m was observed on 23rd June 2018 June after months of high rainfall levels from 2018 March where Kibingor Primary School experienced a high of 250 mm/yr in 2018 April while Perkerra Agri. Research Stn. received a maximum of approximately 120 mm.yr. The crustal subsidence persisted to 2018 August when the rainfall levels drastically dropped, leading to reduced hydrologic loading.

In 9th April of 2019, a maximum upward crustal vertical displacement to 1206.479 m was observed due to the preceding months with low rainfall levels. However, this is quickly succeeded by a continuous subsidence due to the continuous rains, with the vertical amplitude continually fluctuating due to the varying rainfall levels that cause varying hydrological loading on the crust. There was a difference 0.033 m vertical amplitude.

KYN7



A



B

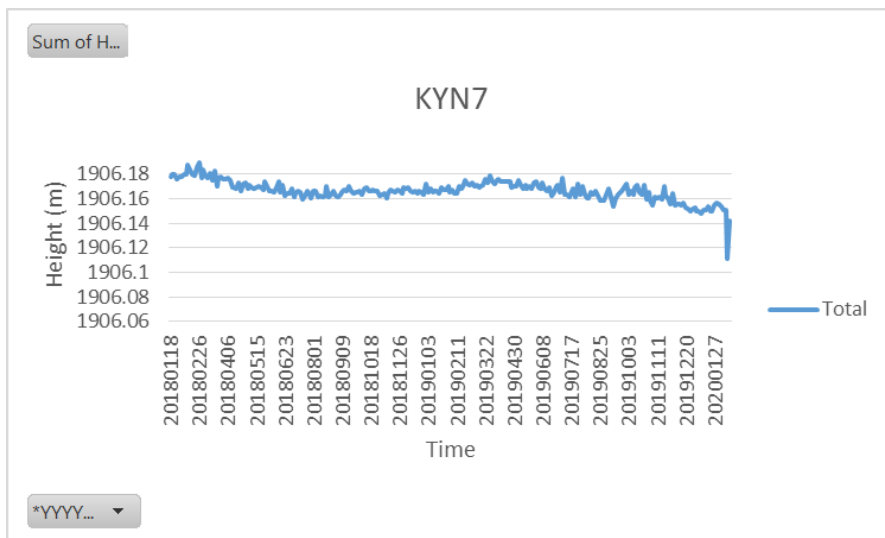


Figure 4.7 A and B showing rainfall in mm/yr against time for locations close to KYN7 GNSS station while C shows KYN7's position estimate time series height in meters against time

Like KYN5, KYN7 experienced the same phenomenon of experiencing a generous rainfall level from 2017 to 2021 with fewer months of little rainfall. Maximum subsidence to 1906.15 m was observed in 2020 21st to 24th January after a season of continuous moderate rainfall from 2019 March with Njoro Ogilgei and Menengai Farm both experiencing a high rainfall level of approximately 230 mm/yr in 2019 December.

However, the maximum crustal upwarp to 1906.184 m is seen in 2018 4th March when both rainfall stations recorded low rainfall levels from 2017 December to 2018 February. Therefore, there is an observed delayed crustal subsidence caused by the rainfall in 2018 March.

There was a difference 0.034 m vertical amplitude.

4.2 Discussion

4.2.1 Velocity Break-Up Rates between the Somalian Plate and the Victoria Microplate and Trends

The EARS accommodates high strain extensions in fault-bounded rifts and low strain extension in highlands (Knappe et al., 2020). While there have been past works written on geodetic extension rates with movements relative to Nubia-Somalia models, this written work is based on the Victoria-Somalia tectonic model. It was found that the NKR GNSS stations, XTBI and XTBT, portray slower velocity break-up rates compared to the GNSS stations in the CKR. While XTBT is in the south of XTBI, it shows slower extension rates of 0.8 ± 0.1 mm/yr in the southeastern direction while XTBI shows a velocity break-up rate of 2.1 ± 0.1 mm/yr in the northwestern direction. In contrast, the GNSS stations in the CKR showed an interesting phenomenon since the break-up velocity rates between the Victoria microplate and the Somalian plate increase southwards. The GNSS station KYN6 experiences 1.7 ± 0.3 mm/yr southwestern extension, KYN4 portrays 1.5 ± 0.1 mm/yr southeastern, KYN3 rifts at 3.0 ± 0.1 mm/yr with a southwestern extension, KYN2 also rifts at 2.0 ± 0.1 mm/yr with a southwestern extension, and finally KYN7 at the furthest south shows an active northeastern extension velocity of 3.3 ± 0.3 mm/yr.

However, the GNSS stations along the Kenyan Rift Valley had a varied spatial distribution where some stations were in the deforming zone while some were in the rigid block zone. The GNSS stations in the deforming zone included XTBI, XTBT, KYN6, KYN4, and KYN7, while KYN3 and KYN2 were in the rigid block zone. The location of these GNSS stations, either in the

deforming or the rigid block zone, had a primary influence on the velocity break-up rates. With this aspect in consideration, in the deforming zone, the break-up velocity rates in the CKR are faster compared to those in the NKR. Unlike what Knappe et al. (2020) and Stamps et al. (2008, 2015) stated, the break-up velocity rates show a southwards increase in the break-up velocity rates in the Turkana Depression. This outcome may possibly be attributed to the varying geodetic tectonic models used in studying the extension rates. However, this significant difference may be based on the previous assumptions due to the lack of adequate GNSS stations coverage in the past to study the extension rates in the CKR. Even so, this trend goes against the Euler pole theorem that tangential extension of break-up velocities increase moving further from the Euler pole (United States Naval Academy, 2022), refuting claims by Knappe et al. (2020) and Stamps et al. (2008, 2015) that geodetic extension rates decrease southwards along the EARS. However, XTBT and KYN7 show unusually faster velocity break-up rates. This could be influenced by mantle tractions beneath the Earth's crust (Rajaonarison et al., 2021), or slipping faults the add divergence to separating tectonic plates (Abbate et al., 1995).

Despite these outcomes, the geographical dynamics along the Kenyan Rift System show a significant variation in topography, which is linked with GPE, an essential input to consider in geodetic extension. The NKR is defined by an extensive Turkana Depression Basin where localized extension along the faults in the area is prominent due to the absence of high topography and therefore low GPE of 4.25×10^{27} Joules. On the other hand, the CKR is defined by high topographies where extensions are accommodated over a long distance (not within constrained faults only) across the highlands, leading to high GPE of 1.45×10^{28} Joules. Hence, this topographical variation, which correlates to GPE variations, have an essential influence in geodetic extension rates, especially in the deforming zones. Therefore, high GPE areas related to high topographies experience high extension rates since extension goes beyond the structural rifts leading to low strain rates as regions without the rift also accommodated the strain (Knappe et al., 2020). This is in line with (Rajaonarison et al., 2021) who agree claiming lithospheric regions with potentially high GPE tend to experience high geodetic extension rates due to the influence of vertical mantle flow. As a result, this vertical mantle flow that derives buoyancy due to varying GPE produces substantial mechanical strength to power tectonic plates diversion (Stamps et al., 2015).

Therefore, based on this, it is evident that the CKR, which is defined by high topographies, has high GPE, unlike the NKR's Turkana Depression, which is a generally flat region. The high GPE in the CKR is thus enough to power faster tectonic diversion between the Victoria microplate and the Somalia plate since extension strain rates go beyond the structural rifts. This is unlike the NKR where rifting strain rates are only accommodated within the regions' structural rifts, leading to slower extension rates.

Vertical displacement due to CWL

The results derived from this study show that precipitation derived from rainfall likely causes systematic solid Earth deflection along the Kenyan Rift System. Thus, the results indicated there is elastic response to CWL, a systematic crustal deflection induced by monsoon precipitation, where hydrological loading due to rainfall leads to geodetic crustal subsidence. This observation extends similarities to studies done in other global parts where GPS had been used to adequately track the Earth's elastic nature as dictated by continental water loading (Birhanu et al., 2018; Birhanu & Bendick, 2015; Jiang et al., 2013). A direct relationship between rainfall and lake level rise was found in that, rainfall increase is sufficient to explain lake level rise (Herrnegger et al., 2021). However, there was an approximate one-month delay between the precipitation occurrence and the crustal subsidence. This delay was a significant factor essentially contributed by the soils' hydraulic properties and how they react with water (Indoria et al., 2020). Therefore, the compared vertical displacement in GPS time series to the rainfall confirmed that the Earth has a varying elastic response due to hydrologic mass transfer, as Knappe et al. (2019) claim.

5. CONCLUSION AND RECOMMENDATIONS

Since the Kenyan Rift is extending due to the divergence between the Victoria microplate and the Somalian plate, there is a significant variation in the systematic deformation between the NKR and CKR. The KYN2 and KYN3 GNSS stations in the rigid zone measured 2.0mm/yr and 3.0mm/yr velocity break-up rates respectively and show consistency with the Somalian plate motion since they are trending in a southwestern direction. In contrast, GNSS station XTBT, which was in a deformation zone, measured 2.1mm/yr velocity rate and shows consistency with the Victoria microplate since it is trending in a northwestern orientation. However, the other GNSS stations, XTBI, KYN4, KYN6, and KYN7, which were also in the deforming zone, measured 0.8mm/yr, 1.5mm/yr, 1.7mm/yr, and 3.3mm/yr velocity break-up rates respectively, show an inconsistent plate motion. This outcome could possibly be attributed to the fact that these GNSS stations were in the deforming zone. As a result, the constraining motions did not align to plate tectonic motions.

To better understand the kinematics and dynamics of the extension rates and trends along the Kenya Rift Valley System, more GNSS stations to constrain plate motion should be installed along the stretch of the Kenyan Rift Valley but not within the deforming zones.

Additionally, the systematic extension accommodation in NKR occurs along a narrow fault bounded region. This is dictated by lack of topographical gradients in the area, leading to a localized rifting along the NKR. As a result, the NKR has a low GPE of 4.25×10^{27} Joules. However, the CKR divergence on the other hand has a different systematic extension due to its high topography that subsequently produces GPE gradients. The high GPE of 1.45×10^{28} Joules in the CKR is due to the presence of a thick crust that provides features for the tectonic accommodation to extend beyond the structural rifts. Therefore, the project suggests that the high GPE in CKR causes a southward increase in the break-up velocity rates. While the same phenomenon is experienced in NKR where velocity break-up rates increase southwards, the faster extension rates for the XTBT and the KYN7 GNSS stations could be due to their positioning in the deforming zone. Therefore, the results indicate that GPE to some extent influence active rifting.

Despite these extension rates along the Kenyan Rift Valley suggesting the importance of GPE in powering plate divergence, the presence of a triple junction close to Lake Bogoria should be considered to determine if it influences rifting in any way. This is because the extension rates

are not consistent with the Euler pole theorem of tangential velocities decreasing towards the Euler pole.

Finally, there was also a time series correlation between the GNSS and the rainfall stations along the Kenyan Rift Valley. The time series showed a consistency in solid Earth response as shown by the GPS time series and rainfall. A period of water loading led to crustal subsidence, as portrayed by downward vertical displacement of the GNSS sites. The reverse occurred with little to no rainfall leading to upward crustal flexure where the Earth's crust experiences upwarping with increased upward amplitude due to reduced CWL. However, there was a lag between rainfall and crustal subsidence possibly attributed to hydrologic soil properties.

Despite the successful accomplishment of the vertical displacement objective, lake levels of the string of lake along the Kenyan Rift System should be monitored to better understand the phenomenon and have intricate correlations between the lakes' level rise, the GNSS time series vertical amplitude variations, and rainfall time series.

REFERENCES

- Abbate, E., Passerini, P., & Zan, L. (1995). Strike-slip faults in a rift area: A transect in the Afar Triangle, East Africa. *Tectonophysics*, 241(1–2), 67–97. [https://doi.org/10.1016/0040-1951\(94\)00136-W](https://doi.org/10.1016/0040-1951(94)00136-W). Accessed 29th November 2022
- Ahn, M., & Geiger, L. C. (1987). *Soils of Laikipia District* (pp. 1–128) [Soil Survey Report]. Ministry of Agriculture. <https://edepot.wur.nl/494202>. Accessed 7th July 2022
- Aktuğ, B., & Yildirim, Ö. (2013). Regularized estimation of Euler pole parameters. *Earth, Planets and Space*, 65(7), 699–705. <https://doi.org/10.5047/eps.2012.10.004>. Accessed 10 November 2022
- Argus, D. F., Fu, Y., & Landerer, F. W. (2014). Seasonal variation in total water storage in California inferred from GPS observations of vertical land motion: Argus et al.: California Water from GPS. *Geophysical Research Letters*, 41(6), 1971–1980. <https://doi.org/10.1002/2014GL059570>. Accessed 6th June 2022
- Avery, S. (2020). Kenya’s Rift Valley lakes have been this high before. But there’s cause for concern. *The Conversation*. <https://theconversation.com/kenyas-rift-valley-lakes-have-been-this-high-before-but-theres-cause-for-concern-147476>. Accessed 10th July 2022
- Baraka, C. (2022). A drowning world: Kenya’s quiet slide underwater. *The Guardian*. <https://www.theguardian.com/world/2022/mar/17/kenya-quiet-slide-underwater-great-rift-valley-lakes-east-africa-flooding>. Accessed 10th July 2022
- Baringo County. (2013). *First County Integrated Development Plan* (pp. 1–277) [County Integrated Development Plan]. Baringo County, Government of Kenya. https://www.baringo.go.ke/images/downloads/Budget_Documents/BARINGO_COUNTY_CIDP.pdf. Accessed 10th May 2022
- Birhanu, Y., & Bendick, R. (2015). Monsoonal loading in Ethiopia and Eritrea from vertical GPS displacement time series: Ethiopia Seasonal Loading. *Journal of Geophysical Research: Solid Earth*, 120(10), 7231–7238. <https://doi.org/10.1002/2015JB012072>. Accessed 16th June 2022
- Birhanu, Y., Wilks, M., Biggs, J., Kendall, J.-M., Ayele, A., & Lewi, E. (2018). Seasonal patterns of seismicity and deformation at the Alutu geothermal reservoir, Ethiopia, induced by hydrological

- loading. *Journal of Volcanology and Geothermal Research*, 356, 175–182. <https://doi.org/10.1016/j.jvolgeores.2018.03.008>. Accessed 16th June 2022
- Blewitt, G., & Lavallée, D. (2002). Effect of annual signals on geodetic velocity: Effect Of Annual Signals On Velocity. *Journal of Geophysical Research: Solid Earth*, 107(B7), ETG 9-1-ETG 9-11. <https://doi.org/10.1029/2001JB000570>. Accessed 16th June 2022
- Bott, M. H. P. (1981). Crustal Doming and the Mechanism of Continental Rifting. In *Developments in Geotectonics* (Vol. 17, pp. 1–8). Elsevier. <https://doi.org/10.1016/B978-0-444-41956-9.50005-8>. Accessed 11th September 2022
- Chorowicz, J. (2005). The East African rift system. *Journal of African Earth Sciences*, 43(1–3), 379–410. <https://doi.org/10.1016/j.jafrearsci.2005.07.019>. Accessed 12th May 2022
- Conti, P., Pistis, M., Bernardinetti, S., Barbagli, A., Zirulia, A., Serri, L., Colonna, T., Guastaldi, E., & Ghiglieri, G. (2021). Tectonic Setting of the Kenya Rift in the Nakuru Area, Based on Geophysical Prospecting. *Geosciences*, 11(2), 80. <https://doi.org/10.3390/geosciences11020080>. Accessed 10th October 2022
- Corti, G., Agostini, A., Keir, D., Van Wijk, J., Bastow, I. D., & Ranalli, G. (2015). Magma-induced axial subsidence during final-stage rifting: Implications for the development of seaward-dipping reflectors. *Geosphere*, 11(3), 563–571. <https://doi.org/10.1130/GES01076.1>. Accessed 10th October 2022
- County Government of Marsabit. (2013). *First County Development Integrated Plan* (pp. 1–284) [Integrated Development Report]. County Government of Marsabit. <https://www.kpda.or.ke/documents/CIDP/Marsabit.pdf>. Accessed 13th June 2022
- Earthview Geoconsultants Limited. (2008). *Environment Impact Assessment of the Proposed Oil and Gas Exploration in Block 10A, Northern Kenya for Lundin Kenya B.V.* (pp. 1–168) [Environment Impact Assessment Report]. Earthview Geoconsultants Limited. <https://www.tulloil.com/application/files/9415/8490/6409/lundin-eia-report--block-10a-seismic.pdf>. Accessed 20th June 2022

- Ebinger, C. (2005). Continental break-up: The East African perspective. *Astronomy and Geophysics*, 46(2), 2.16-2.21. <https://doi.org/10.1111/j.1468-4004.2005.46216.x>. Accessed 25th May 2022
- Feibel, C. S. (2011). A Geological History of the Turkana Basin. *Evolutionary Anthropology: Issues, News, and Reviews*, 20(6), 206–216. <https://doi.org/10.1002/evan.20331>. Accessed 6th June 2022
- Floyd, M. A., & Herring, T. A. (2020). *GNSS data from receiver to processing input*. 2020 SAGE/GAGE Workshop, Massachusetts Institute of Technology, Cambridge, MA, USA. Accessed 26th June 2022
- Githaiga, K. B., Njuguna, S. M., & Yan, X. (2021). Local Geochemical Baselines Reduce Variation Caused by the Use of Different Conservative Elements in Predicting Cu and Zn Enrichment in Agricultural Soils, Kenya. *Chemistry Africa*, 4(4), 869–880. <https://doi.org/10.1007/s42250-021-00256-6>. Accessed 20th August 2022
- Henry, W. J., Mechie, J., Maguire, P. K. H., Khan, M. A., Prodehl, C., Keller, G. R., & Patel, J. (1990). A Seismic Investigation of the Kenya Rift Valley. *Geophysical Journal International*, 100(1), 107–130. <https://doi.org/10.1111/j.1365-246X.1990.tb04572.x>. Accessed 1st September 2022
- Herring, T. A., R. W., Floyd, M. A., & McClusky, S. C. (2018). *Introduction to GAMIT/GLOBK Release 10.7*. http://geoweb.mit.edu/gg/Intro_GG.pdf. Accessed 26th June 2022
- Herrnegger, M., Stecher, G., Schwatke, C., & Olang, L. (2021). Hydroclimatic analysis of rising water levels in the Great rift Valley Lakes of Kenya. *Journal of Hydrology: Regional Studies*, 36, 100857. <https://doi.org/10.1016/j.ejrh.2021.100857>. Accessed 3rd June 2022
- HyperPhysics. (2016). *Gravitational Potential Energy*. <http://hyperphysics.phy-astr.gsu.edu/hbase/gpot.html>. Accessed 29th November 2022
- Indoria, A. K., Sharma, K. L., & Reddy, K. S. (2020). Hydraulic properties of soil under warming climate. In *Climate Change and Soil Interactions* (pp. 473–508). Elsevier. <https://doi.org/10.1016/B978-0-12-818032-7.00018-7>. Accessed 5th October 2022

Institute of Hydrology. (n.d.). *Gorundwater Conditions in Baringo County District, Kenya* (pp. 1–26) [Geological Report]. Accessed 2nd June 2022

Jiang, W., Li, Z., van Dam, T., & Ding, W. (2013). Comparative analysis of different environmental loading methods and their impacts on the GPS height time series. *Journal of Geodesy*, 87(7), 687–703. <https://doi.org/10.1007/s00190-013-0642-3>. Accessed 17th May 2022

Jörges, B., & López-Moliner, J. (2020). Determining mean and standard deviation of the strong gravity prior through simulations. *PLOS ONE*, 15(8), e0236732. <https://doi.org/10.1371/journal.pone.0236732>. Accessed 3rd June 2022

Kasabuli, B. I. (2016). *Environmental Impact Assessment for Bakuli 4 Dam Project and Introduction of Sewerage System in Marsabit County* (pp. 1–216) [Environmental Impact Assessment Report]. Marsabit County. https://www.nema.go.ke/images/Docs/EIA_1340-1349/EIA%201328_%20Bakuli%204%20Dam%20Project%20Report-mini.pdf. Accessed 3rd June 2022

Keen, C. E. (1985). The dynamics of rifting: Deformation of the lithosphere by active and passive driving forces. *Geophysical Journal International*, 80(1), 95–120. <https://doi.org/10.1111/j.1365-246X.1985.tb05080.x>. Accessed 6th May 2022

Key. (1987). *Geology of the Marsabit Area* (Geological Report No. 108; pp. 1–48). Ministry of Environment and Natural Resources Mines and Geological Department. <https://s3-eu-west-1.amazonaws.com/samsamwater1/maps/kenya/geology/Geology+of+the+Marsabit+Area.pdf>. Accessed 6th August 2022

Knappe, E., Bendick, R., Ebinger, C., Birhanu, Y., Lewi, E., Floyd, M., King, R., Kianji, G., Mariita, N., Temtime, T., Waktola, B., Deresse, B., Musila, M., Kanoti, J., & Perry, M. (2020). Accommodation of East African Rifting Across the Turkana Depression. *Journal of Geophysical Research: Solid Earth*, 125(2). <https://doi.org/10.1029/2019JB018469>. Accessed 28th July 2022

Knappe, E., Bendick, R., Martens, H. R., Argus, D. F., & Gardner, W. P. (2019). Downscaling Vertical GPS Observations to Derive Watershed-Scale Hydrologic Loading in the Northern Rockies. *Water Resources Research*, 55(1), 391–401. <https://doi.org/10.1029/2018WR023289>. Accessed 6th August 2022

- Leat, P. T. (1991). Volcanological development of the Nakuru area of the Kenya rift valley. *Journal of African Earth Sciences (and the Middle East)*, 13(3–4), 483–498. [https://doi.org/10.1016/0899-5362\(91\)90111-B](https://doi.org/10.1016/0899-5362(91)90111-B). Accessed 19th July 2022
- Makinouchi, T., Koyaguchi, T., Matsuda, T., Mitsushio, H., & Ishida, S. (1984). *Geology of the Nachola Area and the Samburu Hills, West of Baragoi, Northern Kenya*. The Research Committee for African Area Studies, Kyoto University. <https://doi.org/10.14989/68318>. Accessed 19th July 2022
- Mason, P. (2007). *Geology of the Meru-Isiolo Area* (pp. 1–30) [Geological Report]. Ministry of Environment and Natural Resources Mines and Geological Department. <https://s3-eu-west-1.amazonaws.com/samsamwater1/maps/kenya/geology/Geology+of+the+Meru+Isiolo+area.pdf>. Accessed 19th July 2022
- May, S. (2014). What Is a Satellite? In NASA. <https://www.nasa.gov/audience/forstudents/5-8/features/nasa-knows/what-is-a-satellite-58.html>. Accessed 16th October 2022
- McCall, G. (1967). *Geology of the Nakuru—Thompson’s Falls—Lake Hannington Area* (Geological Report No. 78; pp. 1–143). Ministry of Natural Resources, Geological Survey of Kenya. <https://edepot.wur.nl/493285>. Accessed 19th July 2022
- Milliner, C., Materna, K., Bürgmann, R., Fu, Y., Moore, A. W., Bekaert, D., Adhikari, S., & Argus, D. F. (2018). Tracking the weight of Hurricane Harvey’s stormwater using GPS data. *Science Advances*, 4(9), eaau2477. <https://doi.org/10.1126/sciadv.aau2477>. Accessed 12th September 2022
- Ministry of Environment and Forestry. (2022). *Multi-Agency Team to Combat Rising Water Levels in Rift Valley*. Ministry of Environment and Forestry. <http://www.environment.go.ke/?p=8046>. Accessed 26th September 2022
- Moore, D. (2021). *Climate Change could Spark Floods in World’s Largest Desert Lake: New Study* (Support for Effective Cooperation and Coordination of the Cross-Border Initiatives in Southwest Ethiopia-Northwest Kenya, Marsabit-Borana and Dawa, and Kenya-Somalia-Ethiopia (SECCCI)” Project). United Nations Environmental Programme. <https://www.unep.org/news-and-stories/story/climate-change-could-spark-floods-worlds-largest-desert-lake-new-study>. Accessed 19th July 2022

Muita, R., Gikungu, D., Aura, S., & Njogu, A. (2021). Assessment of Rising Water Levels of Rift Valley Lakes in Kenya: The Role of Meteorological Factors. *Environmental Sciences and Ecology: Current Research (ESECR)*, 2(6), 1–9. <https://doi.org/10.54026/ESECR/1035>. Accessed 20th May 2022

National Geographic. (2022). *Rift Valley*. <https://education.nationalgeographic.org/resource/rift-valley>. Accessed 26th October 2022

Nippon Koei Co., Ltd. & Nihon Suido Consultants CO., Ltd. (1997). *The Study on the Water Supply for Seven Towns in Eastern Province in the Republic of Kenya* (pp. 1–63) [Water Supply Supporting Report]. Japan International Cooperation Agency and The Ministry of Land Reclamation, Regional and Water Development, The Republic of Kenya. https://openjicareport.jica.go.jp/pdf/11403938_01.pdf. Accessed 19th July 2022

Pagli, C., Mazzarini, F., Keir, D., Rivalta, E., & Rooney, T. O. (2015). Introduction: Anatomy of rifting: Tectonics and magmatism in continental rifts, oceanic spreading centers, and transforms. *Geosphere*, 11(5), 1256–1261. <https://doi.org/10.1130/GES01082.1>. Accessed 25th May 2022

Prodehl, C., Fuchs, K., & Mechie, J. (1997). Seismic-refraction studies of the Afro-Arabian rift system—A brief review. *Tectonophysics*, 278(1–4), 1–13. [https://doi.org/10.1016/S0040-1951\(97\)00091-7](https://doi.org/10.1016/S0040-1951(97)00091-7). Accessed 27th November 2022

Rajaonarison, T. A., Stamps, D. S., & Naliboff, J. (2021). Role of Lithospheric Buoyancy Forces in Driving Deformation in East Africa From 3D Geodynamic Modeling. *Geophysical Research Letters*, 48(6). <https://doi.org/10.1029/2020GL090483>. Accessed 23rd September 2022

Randel, R. P. (1970). *Geology of the Laisamis Area* (No. 84; p. 27). Ministry of Natural Resources, Geological Survey of Kenya. <https://s3-eu-west-1.amazonaws.com/samsamwater1/maps/kenya/geology/Geology+of+the+laisamis+area.pdf>. Accessed 19th July 2022

Rédaction Africanews. (2021). Intense rainfall adds to increase in lakes levels in East Africa. *Africa News*. <https://www.africanews.com/2021/08/02/intense-rainfall-adds-to-increase-in-lakes-levels-in-east-africa/>. Accessed 10th July 2022

Riedl, S., Melnick, D., Mibei, G. K., Njue, L., & Strecker, M. R. (2020). Continental rifting at magmatic centres: Structural implications from the Late Quaternary Menengai Caldera, central Kenya Rift. *Journal of the Geological Society*, 177(1), 153–169. <https://doi.org/10.1144/jgs2019-021>. Accessed 11th August 2022

Ring, U. (2014). *The East African Rift System*. 107(1), 132–146. Accessed 22nd November 2022

Stamps, D. S., Calais, E., Saria, E., Hartnady, C., Nocquet, J.-M., Ebinger, C. J., & Fernandes, R. M. (2008). A kinematic model for the East African Rift. *Geophysical Research Letters*, 35(5), L05304. <https://doi.org/10.1029/2007GL032781>. Accessed 19th June 2022

Stamps, D. S., Iaffaldano, G., & Calais, E. (2015). Role of mantle flow in Nubia-Somalia plate divergence. *Geophysical Research Letters*, 42(2), 290–296. <https://doi.org/10.1002/2014GL062515>. Accessed 14th May 2022

Stamps, D. S., Saria, E., & Kreemer, C. (2018). A Geodetic Strain Rate Model for the East African Rift System. *Scientific Reports*, 8(1), 732. <https://doi.org/10.1038/s41598-017-19097-w>. Accessed 14th May 2022

Stamps, S. (2021). *Global Navigation Satellite System (GNSS) Overview*. Accessed 14th May 2022

Stein, S. (n.d.). *Simple Euler Poles* [Department of Earth and Planetary Sciences, Northwestern University]. <https://sites.northwestern.edu/sethstein/simple-euler-poles/#:~:text=Definition%3A%20Euler's%20fixed%20point%20theorem,the%20motions%20of%20tectonic%20plates>. Accessed 14th November 2022

Touber, L. (1989). *Landforms and Soils of Samburu District, Kenya: A Site Evaluation for Rangeland Use* (Site Evaluation No. 8; pp. 1–41). The Winand Staring Centre, Wageningen. <https://edepot.wur.nl/300185>. Accessed 20th June 2022

UNAVCO. (n.d.). *What Is Geodesy?* <https://www.unavco.org/what-is/>. Accessed 14th May 2022

United States Naval Academy. (2022). *Euler Poles*. https://www.usna.edu/Users/oceano/pguth/md_help/geology_course/euler_poles.htm#:~:text=The%20tangential%20velocities%20increase%20moving,will%20lie%20on%20small%20circles. Accessed 14th November 2022

USGS. (n.d.). Tracking Change Over Time—Understanding Remote Sensing. In *USGS - Science for a changing world* (pp. 1–4). https://pubs.usgs.gov/gip/133/pdf/RemSens-Student_web.pdf. Accessed 14th May 2022

Wedmore, L. N. J., Biggs, J., Floyd, M., Fagereng, Å., Mdala, H., Chindandali, P., Williams, J. N., & Mphepo, F. (2021). Geodetic Constraints on Cratonic Microplates and Broad Strain During Rifting of Thick Southern African Lithosphere. *Geophysical Research Letters*, *48*(17). <https://doi.org/10.1029/2021GL093785>. Accessed 18th November 2022

APPENDICES

Appendix A: General practice for NetR9's GNSS data download procedure is:

- 1) Connect to the receiver using an ethernet cable
- 2) Set the IP address of your computer to be have the same first 3 numbers as the receiver, the last number must be different.
- 3) Make a directory on your machine to download the data to “mkdir <directory_name>”
- 4) Go into the directory you just made “cd <directory_name>”
- 5) ftp into the receiver "ftp <reciever IP address>”
- 6) Go to the place on the reciever where the data is “cd Internal/<path/to/data/>”

This will vary depending on the how a receiver is set up. For the UM receivers the data is generally in Internal/yyyymm/a

Just navigate around the reciever in the terminal if you are confused, using “ls”, “cd”, “pwd”, etc.

- 7) To download the data, “mget *T02”

This will download all files that end in “T02” to the directory on the computer you ftp'd from.

- 8) Change directories to other places and download other data

for example: “cd Internal/201901/a” (this is an example of step 6)

“mget *T02” (this is an example of step 7)

“cd ../../201901/a”

“mget *T02”

“cd ../../201902/a”

Etc.

Appendix B: Processing using GAMIT/GLOBK

Virginia Tech computer (at gtl.geos.vt.edu) was accessed virtually for the processing because of space and speed.

In the processing space, in linux, a directory was created for the project and named [keny](#).

First, the set up was done for all the processing years from 2017 to 2021 using the command `sh_setup -yr <year>`

In every year directory, there was a RINEX directory, in which every stations' RINEX files were downloaded, including those for the reference stations.

After cross checking that the station.info and sites.default had all the necessary and correct information for all sites, GAMIT, which was the first step of the processing, was run.

`Sh_gamit -expt kenya -s <yr> 001 365 -orbit igsf -pres ELEV -copt x k p`

Sh_gamit conducts phase processing for separate GNSS (in this case GPS) and creates each day's directories after successful processing.

What everything in the sh_gamit command means

sh_gamit – this is the command that tells the program to run GAMIT (phase processing)

-expt – this denotes the experiment (in this case 'kenya')

-s – this is the period that sh_gamit is processing (say 2018' what follows after, say 001 366, these are the days of the years processing)

-pres ELEV – default command to plot phase vs elevation as skyplots

-orbit – this denotes the type of orbit used in the processing (in this case, the igsf is used as the default. F in igsf is for precision, in millimeters)

-copt – denotes the list of files to compress in the day directory (the x, k, and p files which are automatically saved. x-files are for observation while the k-files are the receiver-clock estimates)

>& sh_gamit_2018.log & - a file where the record of each step during the processing is written.

The & at the end of the command allows the processing to go on at the background

After successfully running GAMIT, the second step was to run GLOBK for repeatabilities and getting the H-files for the period processed.

At the year level, in each directory, the command `sh_glred -cmd` was ran in order to get the `globk.cmd` and `glorg.cmd` files copied in the 2018/gsoln from the `gg/tables`.

The command used for this process was `Sh_glred -s 2018 001 2018 365 -expt kenya -opt R H G T >& sh_glred.log`.

This step did three things; 1, the H-option tells glred to translate the daily GAMIT ascii h-files into GLOBK binary h-files (.glx) that are then put in the glbf directory, 2, the G-option instructs glred to be run and create a `gdl` file listing of everyday h-files and run GLOBK for each day using `globk.cmd` and `glorg.cmd`, and finally 3, the T-option, generates time series plots using `pos` files, program `tssum` and `sh_plot_pos`.

The next step was to combine the daily h-files for a single 3-day H-file combinations of the whole year. These H-files will be later used for time series (multi-year) repeatabilities and velocities.

The command used for this step was `Sh_glred -s 2019 001 2019 365 -expt kenya -ncomb 3 -globk_cmd_prefix COMB -opt G >&sh_glred_comb.log`.

The fourth step involved running GLOBK to get the 5-year epoch repeatabilities and velocities.

The command used was `ls ../????/gsoln/H*GLX > kenya.gdl` to create a combined h-files list for `globk`.

This command was followed by the command `glred 6 globk_replong.prt globk_replong.log kenya.gdl globk.cmd >& glred.out`.

This step was succeeded by the command `tssum . gtl.final.igs14 -R *.org`, in the `vsoln` directory to create the `pos` files for plotting.

To finally make the multi-year plots from the previously made `pos` files, the command `sh_plot_pos -f *.pos` was ran.

Finally, to get velocities from the -year processing, this command was ran

`globk 6 globk_vel.prt globk_vel.log kenya.gdl globk.cmd VEL >& globk.out` and the file output in the `vsoln` directory for this command was `glred_dl----.vel`.

Then the file (glred_dl----.vel) was converted to a psvelo file to make it possible to plot the horizontal displacements on the vector map using GMT. To convert it to a psvelo file, the command `./vel2psvelo glred_dl----.vel velocity_hz velocity_vt` was used (however, a `vel2psvelo.sh` executable file (in the image below) had to be created first to successfully do the conversion)

```
#!/bin/tcsh
if ($#argv < 3) then
  echo ""
  echo "This script will convert a globk velocity file into psvelo file"
  echo ""
  echo "usage: [file] [file_name_horizontal] [file_name_vertical]"
  echo ""
  echo "[1] [file] = file in globk velocity format"
  echo "[2] [test] = file name without .psvelo"
  echo "[3] [test] = file name without .psvelo"
  echo ""
exit
endif

# General definitions
set horz = "$2"
set vert = "$3"
set file = "$1"

# Do the conversion
awk '/(deg)/,eof' $file | awk 'NR>1' > tmp
awk '{print $1,$2,$3,$4,$7,$8,$9,$13}' tmp > $horz.psvelo
awk '{print $1,$2,0,$10,0,$12,0,$13}' tmp > $vert.psvelo
rm tmp

echo "Finished creating:"
echo ""
echo "$horz.psvelo"
echo "$vert.psvelo"
```

The executable `vel2psvelo.sh` file used to convert the `glred_dl----.vel` file to both `velocity_hz.psvelo` and `velocity_vt.psvelo` files

Appendix C: Using the rot program to place extension velocities in the Victoria-Nubia plate reference frame

To commence putting the velocities in a Victoria-Nubia plate reference frame, in the rot directory, a file called kenya.psvelo was created where all these sites from the original velocity_hz.psvelo file were grep'd.

The command used was

```
grep XTBT velocity_hz.psvelo > kenya.psvelo
```

```
grep XTBI velocity_hz.psvelo >> kenya.psvelo
```

 (This command was followed through for the other sites too; KYN2, KYN3, KYN4, KYN6, KYN7, and MAL2)

Rot was then run, choosing option 2 which is a Rotation vector (Rx,Ry,Rz) format. Line148 was used (Nubi itrf14 altamimi17 0.027499 -0.17055 0.203611 0 0 0 0 0 0 0) in the rotation.dat file, which has various Euler parameters for varying plates.

The input file was the kenya.psvelo and the output file was nub_wrt_itrf_altamimi_kenya.psvelo. The sites in nub_wrt_itrf_altamimi_kenya.psvelo were now in the predicted Nubian plate motion relative to International Time Reference Frame (itrf).

However, to get this new velocity file into a Nubian reference frame, these predicted coordinates in the nub_wrt_itrf_altamimi_kenya.psvelo file were subtracted from those in kenya.psvelo file.

The command used for this was

```
paste kenya.psvelo nub_wrt_itrf_altamimi_kenya.psvelo | awk '{print $1, $2, $3-$11, $4-$12, $5, $6, $7, $8}' > awk_nub_wrt_itrf_altamimi_kenya.psvelo, and  
awk_nub_wrt_itrf_altamimi_kenya.psvelo was the output. Therefore, the sites in this file (awk_nub_wrt_itrf_altamimi_kenya.psvelo) were in a Nubian fixed reference frame.
```

However, the sites velocities' needed to be in the Victoria fixed reference frame. To do this, the Victoria plate motion needed to be subtracted from the ones in awk_nub_wrt_itrf_altamimi_kenya.psvelo. This output would be Victoria relative to Nubia.

So the rot program was ran again using the same procedure again, but this time in the rotation.dat file, line 142 was used (nubi vict stamps21 D 0.0626 0.0400 0.0160 0.0000 0.0000 0.0000 0.0000 0.0000 0.0000).

The input file was `keny.psvelo`, and the output file was `nub_wrt_vic_stamps21_keny.psvelo`.

Now, the velocities in `nub_wrt_vic_stamps21_keny.psvelo` were subtracted from those in `awk_nub_wrt_itrf_altamimi_keny.psvelo` using the command

```
paste awk_nub_wrt_itrf_altamimi_keny.psvelo nub_wrt_vic_stamps21_keny.psvelo | awk '{print $1, $2, $3-$11, $4-$12, $5, $6, $7, $8}' > awk_nub_wrt_vic_keny.psvelo.
```

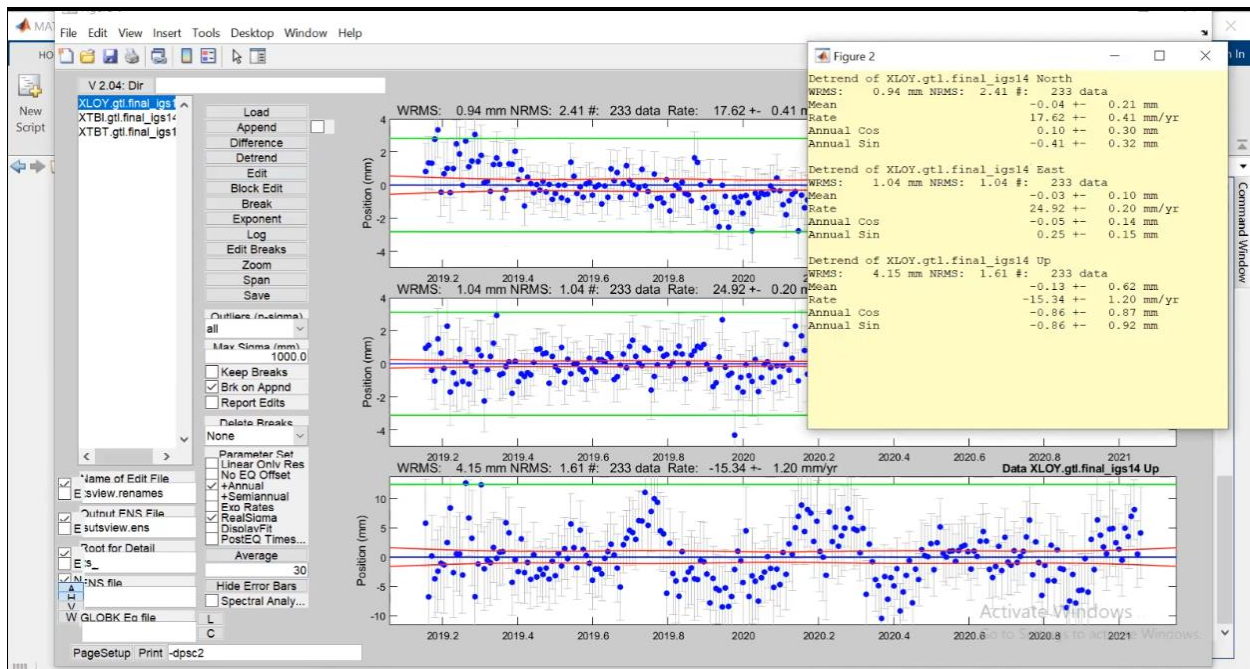
The output from running this command was `awk_nub_wrt_vic_keny.psvelo`.

Appendix D: How to check for seasonality with tsview

To test for the presence of various signals in a station position time series file, the station position time series file for one station was ran four times to test for signals. The first time the position time series file was processed without a signal, then with an annual signal, followed by a semiannual signal, and finally with both annual and semiannual signals selected. However, throughout the four processing phases, the real sigma box was checked with the assumption that the signals had a real sigma component, which is time correlated noise (χ^2/f).

After successfully loading a site's station position time series file and selecting the signal to process, the detrend button was clicked. The detrend option is an iterative process that removes the outlier data alongside offsets and linear rates at breaks.

A yellow box that has the North, East, and Up components pop up, but only the Up component that helps detect seasonality in the vertical displacement was of interest.



For each site's station position time series file, four signals were plotted against their output WRMS.

Appendix E: Calculation of Errors for Extension Velocities

SITES	σ_e	σ_n	$\sigma_e.sq$	$\sigma_n.sq$	$\sigma_e.sq+\sigma_n.sq$	$\sqrt{(\sigma_e.sq+\sigma_n.sq)}$	ERRORS
XTBT_G PS	0.05	0.04	0.0025	0.0016	0.0041	0.064031242	±0.1
XTBI_GP S	0.08	0.07	0.0064	0.0049	0.0113	0.106301458	±0.1
KYN2_G PS	0.09	0.08	0.0081	0.0064	0.0145	0.120415946	±0.1
KYN3_G PS	0.1	0.08	0.01	0.0064	0.0164	0.128062485	±0.1
KYN4_G PS	0.11	0.09	0.0121	0.0081	0.0202	0.142126704	±0.1
KYN6_G PS	0.19	0.17	0.0361	0.0289	0.065	0.254950976	±0.3
KYN7_G PS	0.2	0.17	0.04	0.0289	0.0689	0.262488095	±0.3
MAL2_3 PS*	0.07	0.06	0.0049	0.0036	0.0085	0.092195445	±0.1